JPL D-13401, Rev. D

Earth Observing System

MISR

Multi-angle Imaging Spectro-Radiometer

Level 2 Top-of-Atmosphere Albedo Algorithm Theoretical Basis

David J. Diner[1]
Roger Davies[2]
Tamas Várnai[2]
Catherine Moroney[2]
Christoph Borel[3]
Siegfried A. W. Gerstl[3]
David L. Nelson[1]

[1]Jet Propulsion Laboratory, California Institute of Technology
[2]University of Arizona
[3]Los Alamos National Laboratory

JPL

Jet Propulsion Laboratory
California Institute of Technology

November 2, 1999

JPL D-13401, Rev. D

Multi-angle Imaging SpectroRadiometer (MISR)

Level 2 Top-of-Atmosphere Albedo Algorithm Theoretical Basis

Approval:

David J. Diner
MISR Principal Investigator

The MISR web site should be consulted to determine the latest released version
of this document (http://www-misr.jpl.nasa.gov).
Approval signatures are on file with the MISR Project.

JPL

Jet Propulsion Laboratory
California Institute of Technology

TABLE OF CONTENTS

GLOSSARY OF ACRONYMS

A

AGP (Ancillary Geographic Product)
ARP (Ancillary Radiometric Product)
ASCM (Angular Signature Cloud Mask)
ATB (Algorithm Theoretical Basis)
AVHRR (Advanced Very High Resolution Radiometer)
AZM (Azimuthal Model)

B

BRDF (Bidirectional Reflectance Distribution Function)
BRF (Bidirectional Reflectance Factor)

C

CCD (Charge-Coupled Device)
ClearHC (Clear with High Confidence)
ClearLC (Clear with Low Confidence)
CloudHC (Cloud with High Confidence)
CloudLC (Cloud with Low Confidence)
CSAR (Coupled Surface-Atmosphere Reflectance)
CSSC (Cloud Screening Surface Classification)

D

DAAC (Distributed Active Archive Center)
DAO (Data Assimilation Office)
DHR (Directional Hemispherical Reflectance)

E

EOS (Earth Observing System)
ERBE (Earth Radiation Budget Experiment)

F

FOV (Field-of-View)

H

HRC (Homogeneity Reference Camera)

I

IFOV (Instantaneous Field Of View)

IR (Infrared)
ISCCP (International Satellite Cloud Climatology Project)

J

JPL (Jet Propulsion Laboratory)

L

LAC (Local Area Coverage)

M

MC (Monte Carlo)
MISR (Multi-angle Imaging SpectroRadiometer)
MODIS (Moderate Resolution Imaging Spectroradiometer)

N

NR (No Retrieval)
NSIDC (National Snow and Ice Data Center)

R

RLRA (Reflecting Level Reference Altitude)
RMS (Root-Mean-Square)

S

SCF (Science Computing Facility)
SDCM (Stereoscopically Derived Cloud Mask)

T

TASC (Terrestrial Atmosphere and Surface Climatology)
TOA (Top-of-Atmosphere)

W

WGS (World Geodetic System)

1. INTRODUCTION

1.1   PURPOSE

This Algorithm Theoretical Basis (ATB) document describes the algorithms used to retrieve the albedo parameters of the Multi-angle Imaging SpectroRadiometer (MISR) Level 2 Top-of-Atmosphere (TOA)/Cloud Product. These parameters are summarized in Table 1. The TOA/Cloud Product also contains a number of parameters used to classify clouds. The derivation of those parameters is described in *[M-8]* (see reference list below).

In particular, this document identifies sources of input data, both MISR and non-MISR, required for parameter retrievals; provides the physical theory and mathematical background underlying the derivation of TOA/cloud albedo parameters; includes implementation details; and describes assumptions and limitations of the adopted approach. It is used by the MISR Science Data System Team to establish requirements and functionality of the data processing software.

Table 1: Top-of-atmosphere albedo parameters in the Level 2 TOA/Cloud Product

Parameter name	Units	Horizontal Sampling and Coverage	Comments
TOA albedo - local	none	2.2 km (Global)	• Unobscured spectral directional hemispherical reflectance at reflecting-level reference altitude (RLRA) • 4 spectral bands
Subregion classifiers for local albedo	none	2.2 km (Global)	• Includes: -- surface type -- cloudy/clear indication -- cloud phase -- high cloud presence -- cloud texture -- other ancillary data for retrieval pathway determination and quality assessment
TOA albedo - restrictive	none	35.2 km (Global)	• Unobscured spectral directional hemispherical reflectance • 4 spectral bands • Sampled from single region only
TOA albedo - expansive	none	35.2 km (Global)	• Spectral directional hemispherical reflectance • 30 km (above WGS84 ellipsoid) reference altitude • 4 spectral bands • Sampled from all relevant regions
Expansive albedo classifiers	none	35.2 km (Global)	• Fraction of the area over which expansive albedo is calculated that is clear with high confidence, and clear with low confidence

1.2 SCOPE

This document covers the algorithm theoretical basis for the albedo parameters of the TOA/Cloud Product which are to be routinely retrieved at the DAAC. Post-launch and specialized products or parameters are not discussed. Current development and prototyping efforts may result in modifications to parts of certain algorithms. Only the algorithms which will be implemented at the DAAC for routine processing will be preserved in the final release of this document.

This document also covers the algorithm theoretical basis for generation of the Azimuthal Model (AZM) Dataset, an ancillary dataset produced at the MISR SCF and delivered to the DAAC for use as input during standard processing. The contents of the AZM Dataset are also provided.

Chapter 1 describes the purpose and scope of the document. Chapter 2 provides a scientific background. The processing concepts and algorithm descriptions for the albedo parameters of the TOA/Cloud Product are presented in Chapter 3 and for the AZM Dataset parameters are presented in Chapter 4. Chapter 5 summarizes assumptions and limitations. References for publications cited in the text are given in Chapter 6. Literature references are indicated by a number in italicized square brackets, e.g., *[1]*.

1.3 MISR DOCUMENTS

Reference to MISR Project Documents is indicated by a number in italicized square brackets as follows, e.g., *[M-1]*. The MISR web site (http://www-misr.jpl.nasa.gov) should be consulted to determine the latest released version of each of these documents.

[M-1] Experiment Overview, JPL D-13407.

[M-2] Level 1 Radiance Scaling and Conditioning Algorithm Theoretical Basis, JPL D-11507.

[M-3] Level 1 Georectification and Registration Algorithm Theoretical Basis, JPL D-11532.

[M-4] Level 1 Cloud Detection Algorithm Theoretical Basis, JPL D-13397.

[M-5] Level 1 In-flight Radiometric Calibration and Characterization Algorithm Theoretical Basis, JPL D-13398.

[M-6] Level 1 Ancillary Geographic Product Algorithm Theoretical Basis, JPL D-13400.

[M-7] Level 1 In-flight Geometric Calibration Algorithm Theoretical Basis, JPL D-13399.

[M-8] Level 2 Cloud Detection and Classification Algorithm Theoretical Basis, JPL D-11399.

[M-9] Level 2 Aerosol Retrieval Algorithm Theoretical Basis, JPL D-11400.

[M-10] Level 2 Surface Retrieval Algorithm Theoretical Basis, JPL D-11401.

[M-11] Level 2 Ancillary Products and Datasets Algorithm Theoretical Basis, JPL D-13402.

[M-12] Algorithm Development Plan, JPL D-11220.

[M-13] In-flight Radiometric Calibration and Characterization Plan, JPL D-13315.

[M-14] In-flight Geometric Calibration Plan, JPL D-13228.

[M-15] Science Data Validation Plan, JPL D-12626.

[M-16] Science Data Processing Sizing Estimates, JPL D-12569.

[M-17] Science Data Quality Indicators, JPL D-13496.

1.4 REVISIONS

The original version of this document was dated March 3, 1994. Revision A was released December 19, 1994. Revision B was released September 20, 1996. Revision C was released December 9, 1997. This version is Revision D. Changes from Rev. C are indicated through the use of change bars, as shown at the left.

2. EXPERIMENT OVERVIEW

2.1 OBJECTIVES OF MISR TOA/CLOUD ALBEDO RETRIEVALS

As a result of their large areal extent, high albedo, and variability on many timescales, clouds play a major role in governing the Earth's energy balance. Regional studies of the impact of clouds on the energy balance require measurements of the radiation budgets as a function of scene type. The importance of cloud characteristics in global studies of climate has been well documented *[25]*. Current theories and models of the response of the Earth's climate system to, for example, the increase in trace gases, are severely limited by our present ignorance of the feedback processes associated with changes in cloud amount and cloud properties. In this respect, two issues are paramount. One is the realistic modeling of cloud-radiation interaction taking into account the variable structure of broken cloud fields and processes that occur at the sub-grid scale level of present general circulation models. The other is the ability to invert satellite measured radiances to obtain hemispherical fluxes with sufficient resolution to discriminate between cloud-filled and cloud-free scenes.

Deriving from its ability to measure any scene from multiple directions, MISR will contribute unique information on spectral albedos. This will enable study, on a global basis, of the effects of different types of cloud fields (classified by their heterogeneity and altitude) on the spectral solar radiance and irradiance reflected to space, including spatial and temporal dependences. The most important elements of the MISR retrievals are accurate spectral albedos and spectral bidirectional reflectance factors, coupled to useful scene information, such as parameterizations of the cloud morphology.

A scientific background and historical perspective on related cloud studies using remote sensing, the unique contributions of MISR, and a scientific rationale for the cloud classification parameter contents of the MISR TOA/Cloud Product are presented in *[M-1]*.

2.2 INSTRUMENT CHARACTERISTICS

The MISR instrument consists of nine pushbroom cameras. It is capable of global coverage every nine days, and flies in a 705-km descending polar orbit. The cameras are arranged with one camera pointing toward the nadir (designated An), one bank of four cameras pointing in the forward direction (designated Af, Bf, Cf, and Df in order of increasing off-nadir angle), and one bank of four cameras pointing in the aftward direction (using the same convention but designated Aa, Ba, Ca, and Da). Images are acquired with nominal view angles, relative to the surface reference ellipsoid, of 0°, 26.1°, 45.6°, 60.0°, and 70.5° for An, Af/Aa, Bf/Ba, Cf/Ca, and Df/Da, respectively. Each camera uses four Charge-Coupled Device (CCD) line arrays in a single focal plane. The line arrays consist of 1504 photoactive pixels plus 8 light-shielded pixels plus 8 "overclock" samples of the CCD serial register per array, each 21 μm by 18 μm. Each line array is filtered to provide

one of four MISR spectral bands. The spectral band shapes are approximately gaussian and centered at 446, 558, 672, and 866 nm.

MISR contains 36 parallel signal chains corresponding to the four spectral bands in each of the nine cameras. The zonal overlap swath width of the MISR imaging data (that is, the swath seen in common by all nine cameras along a line of constant latitude) is ≥ 360 km, which provides global multi-angle coverage of the entire Earth in 9 days at the equator, and 2 days near the poles. The cross-track IFOV and sample spacing of each pixel is 275 m for all of the off-nadir cameras, and 250 m for the nadir camera. Along-track IFOV's depend on view angle, ranging from 214 m in the nadir to 707 m at the most oblique angle. Sample spacing in the downtrack direction is 275 m in all cameras. The instrument is capable of buffering the data to provide 2 sample x 2 line, 4 sample x 4 line or 1 sample x 4 line averages, in addition to the mode in which pixels are sent with no averaging. The averaging capability is individually selectable within each of the 36 channels, and there are several observational modes of the MISR instrument. The MISR TOA/Cloud Product is generated from Global Mode data. Global Mode refers to continuous operation with no limitation on swath length. Global coverage in a particular spectral band of one camera is provided by operating the corresponding signal chain continuously in a selected resolution mode. Any choice of averaging modes among the nine cameras that is consistent with the instrument power and data rate allocation is suitable for Global Mode. Current plans are to operate the instrument in the 4 x 4 averaging mode (1.1-km sampling) with selected channels operated in 1 x 1 or 1 x 4 mode.

Most of the highest resolution observations will be acquired in the red (672-nm) band, as this is expected to be the wavelength where the imagery will have the highest contrast, based upon considerations of atmospheric haze, land and ocean reflectivity, and instrument performance. These observations are central to the stereoscopic and texture-based approaches to be used as part of MISR cloud classification *[M-8]*.

Additional background on the instrument design is provided in *[M-1]*.

2.3 ALBEDO DEFINITIONS AND RETRIEVAL STRATEGY

The TOA/Cloud Product contains three types of albedos, as shown in Figure 1: Local, restrictive, and expansive. Local albedos are defined for $(2.2\text{-km})^2$ subregions. Restrictive and expansive albedos correspond to $(35.2\text{-km})^2$ regions. Four spectral albedos of each type will be derived, one for each of the four MISR bands. Assuming the correct spectral irradiances are used, the adjective "spectral" is omitted from the following discussion, which applies equally to each spectral band.

The calculation of directional hemispherical reflectance (DHR), or albedo, involves an angular integration of bidirectional reflectance factors (BRF's) over the upwelling hemisphere.

5

MISR's arrangement of nine cameras provides good coverage in zenith angle; however, the fore-aft views provide sampling at only two azimuth angles for each zenith angle. (Denser coverage in azimuth angle would require binning data acquired on different orbits, and thus would not represent an instantaneous view of the same scene). Supplemental information to model the azimuthal dependence of BRF is therefore required to obtain the most accurate estimates of albedo. Each of the nine view directions is assigned to a solid angle "bin"; the sum of the solid angle bins equals 2π sr. Where feasible, the specification of the angular variation of BRF within each solid angle bin is accomplished through the use of azimuthal models (AZM's). The governing philosophy is to keep the processing sufficiently flexible that model results can be used when appropriate without compromising those portions of the albedo product for which the models do not apply. Separate models are developed for clear and cloudy scenes, and both rely on pre-launch information at this stage. The key azimuthal correction is applied to the local albedos, which are then appropriately summed to obtain the restrictive and expansive albedos. The pre-launch processing that establishes the model archive is described in Chapter 4. Since considerable additional statistical information will become available post-launch, at least for some combinations of azimuth and zenith angles, this additional information will ultimately be included as improvements to the azimuthal modeling.

2.3.1   Local albedos

The probability of scene heterogeneity increases rapidly with scene size, making the relationship between area-averaged radiance and area-averaged scene properties (e.g., cloud liquid water) progressively more biased *[20]*. This limitation affects our ability to choose unique azimuthal models for the scene. It also limits the usefulness of reporting albedos as a function of other scene characteristics. Accordingly, the local albedos are evaluated at relatively high resolution, i.e., for $(2.2\text{-km})^2$ subregions.

There may at times be considerable heterogeneity even at 2.2 km resolution. However, use of the original measurements at 275 m resolution allows the presence of such heterogeneity to be identified when it occurs, through the reporting of texture indices (see *[M-8]*).

The two main objectives in creating a local albedo product at high resolution are thus:

  (i) By matching albedos to scene characteristics, especially cloud information, albedos can be obtained as functions of scene type.

  (ii) Local albedos for relatively homogeneous scenes can be corrected for azimuthal bias more effectively than albedos of larger areas. The azimuthally corrected local albedos can then be summed over larger areas to produce restrictive and expansive albedos of more heterogeneous scenes at coarser resolution.

As described in *[M-8]*, a unique reflecting layer reference altitude (RLRA) is determined for each $(2.2\text{-km})^2$ subregion. This reference altitude is derived through a combination of stereoscopic

and radiometric cloud detection algorithms. The RLRA defines the common horizontal surface to which each of the nine measured BRF's are registered by a process of reprojection from the WGS84 surface ellipsoid. This surface ellipsoid is used as a reference for projecting the MISR observations during Level 1B2 processing *[M-3]*. During Level 2 cloud detection and classification processing *[M-8]*, the Level 1B2 ellipsoid-projected radiances are converted to BRF's and reprojected onto the RLRA. Since the RLRA can change discretely in height from one 2.2-km subregion to the next, the reprojection maps data from a continuous 0-km altitude surface to a patchwork of square columns of possibly discontinuous heights. The reprojection results in all measured BRF's being attributed (discretely at the 275 m pixel level) to either an RLRA surface at the top of a column (*top-leaving BRF's*), or to the sides of a column (*side-leaving BRF's*). The side-leaving BRF's are not used in evaluating local albedos, but are saved for later use in the restrictive and expansive albedo calculations. The local albedos are determined entirely from the top-leaving BRF's.

A second consequence of the reprojection to reference surfaces at different heights, directly related to the generation of side-leaving BRF's, is that portions, or all, of some RLRA surfaces are obscured at oblique views. Such obscuration means that a portion of the upwelling irradiance from a lower altitude surface interacts at higher altitude(s) with one or more neighboring regions. Since the obscured portion reappears either in terms of side-leaving BRF's or through a higher RLRA, we do not count it twice, and accordingly *define the local albedo to be the ratio of the **unobscured** upwelling irradiance through the RLRA to the downwelling TOA irradiance above the RLRA*.

This means that there may be a difference between the TOA local albedo (as defined) and the albedo that would be conventionally measured *in situ* at the RLRA, in addition to the usual difference caused by the effects of the clear atmosphere above the RLRA. These albedos may differ for lower RLRA's, but will be the same for higher RLRA's that suffer no obscuration. When we consider the possibility that lower RLRA's can also be shadowed from the direct solar beam by higher altitude neighboring regions, attempts to further reconcile these definitions appears unwarranted, given the two main objectives stated above. Unobscured fractions for each of the nine average BRF's that are used in the local albedo evaluation are stored together with other scene characteristics, so that the degree of obscuration of each local albedo can readily be identified.

2.3.2 Restrictive albedos

The restrictive albedo refers to reflected radiation from surfaces within a $(35.2\text{-km})^2$ region, and is *defined as the ratio of the unobscured irradiance reflected from all surfaces within a $(35.2\text{-km})^2$ region to the downwelling TOA irradiance above that region*. The relevant reflected irradiance is from all RLRA surfaces and column sides within the region that are unobstructed by other regions. Because these surfaces are generally far below the TOA altitude of 30 km, this irradiance emerges through the TOA over a much wider area than the original $(35.2\text{-km})^2$, thereby contributing to an expansive albedo which is defined below.

The restrictive albedo is thus due in part to the sum of the unobscured irradiances already associated with the local albedos from the 256 $(2.2\text{-km})^2$ subregions that make up the $(35.2\text{-km})^2$ coarse resolution region. These irradiances have already been azimuthally corrected using the best technique for each local region, and can be directly added (see §3.5.1.1). The remainder of the restrictive albedo is due to the irradiance contributions of the side-leaving BRF's originating from the sides of columns within the coarse resolution region. These are added for each relevant viewing direction, and their irradiance contribution is determined using solid angle weights. Solid angle weighting implies no azimuthal correction can sensibly be made, which is currently the expectation for side-leaving BRF's.

From a physical perspective, the restrictive albedo is analogous to the average over the $(35.2\text{-km})^2$ region of measurements made by an albedometer at a constant altitude equal to the highest RLRA of the region. It would differ due to the effects of the clear atmosphere above this altitude, and also because of potential obscuration or residual side-leaving BRF effects due to differences in maximum altitude from one region to the next. Obscuration and residual side-leaving differences are much smaller for restrictive albedos than for local albedos.

2.3.3 Expansive albedos

The expansive albedo is similar to the restrictive albedo in that it is referenced to the same $(35.2\text{-km})^2$ region. However, it refers to the entire irradiance field escaping from the atmosphere above that region. The expansive albedo *is defined as the ratio of the upwelling irradiance through a $(35.2\text{-km})^2$ region at the top of atmosphere (30 km altitude) to the downwelling TOA irradiance on that region.* Since all of the irradiance through the TOA is unobscured, this definition is now the same as the conventional definition. The expansive albedo would be identical to the measurements of an albedometer at an altitude of 30 km.

Note, however, that the reflecting surfaces contributing to the upwelling irradiance in this definition may be horizontally distant from the center of the TOA region by anywhere from 0 to hundreds of km. The expansive albedo consequently integrates the effects of variations in scene properties over a much wider area than does the restrictive albedo. This integration over large areas tends to average out abrupt changes in the albedo values, and as a result, expansive albedos have much smoother spatial variations than restrictive albedos. In large homogeneous areas where all regions influencing a particular expansive albedo have identical restrictive albedos, the expansive albedo is exactly equal to the restrictive albedo. In general, however, reflection properties are expected to vary over the area influencing an expansive albedo value. In such cases, the expansive albedo cannot be calculated based on geometrical considerations alone, due to the anisotropy of the reflected radiation. However, since the only difference between the two albedos is in the geographical registration of the same reflected radiation, the global averages of restrictive and expansive albedos are identical.

From a physical perspective, the difference between the expansive and restrictive albedos is symptomatic of scene heterogeneity and implies the need for additional care in interpreting the results in terms of, say, shortwave cloud radiative forcing. The restrictive albedo is determined predominantly by the properties of a $(35.2 \text{ km})^2$ column (the effects of horizontal diffusion between neighboring areas are fairly small), whereas the expansive albedo of a $(35.2 \text{ km})^2$ region is influenced by the properties of an area extending to a few hundred kilometers on each side. As a result, the restrictive albedo is the more useful measure of scene-dependent properties such as columns absorption, and is analogous to earlier single view determinations of the TOA albedo (e.g., ERBE).

(2.2 km)²

RLRA

Top-leaving BRF's

$$A_{\text{local}} = \sum_{k=1}^{9} \delta A_k$$

LOCAL ALBEDO

$A_{\text{local}}(x, y)$

Side-leaving BRF's

$$A_{\text{restrictive}} = \langle A_{\text{local}} \rangle + side\ contributions$$

RESTRICTIVE ALBEDO

35.2 km

30-km altitude

Top- and side-leaving BRF's

$$A_{\text{expansive}} = Top\ contributions + side\ contributions$$
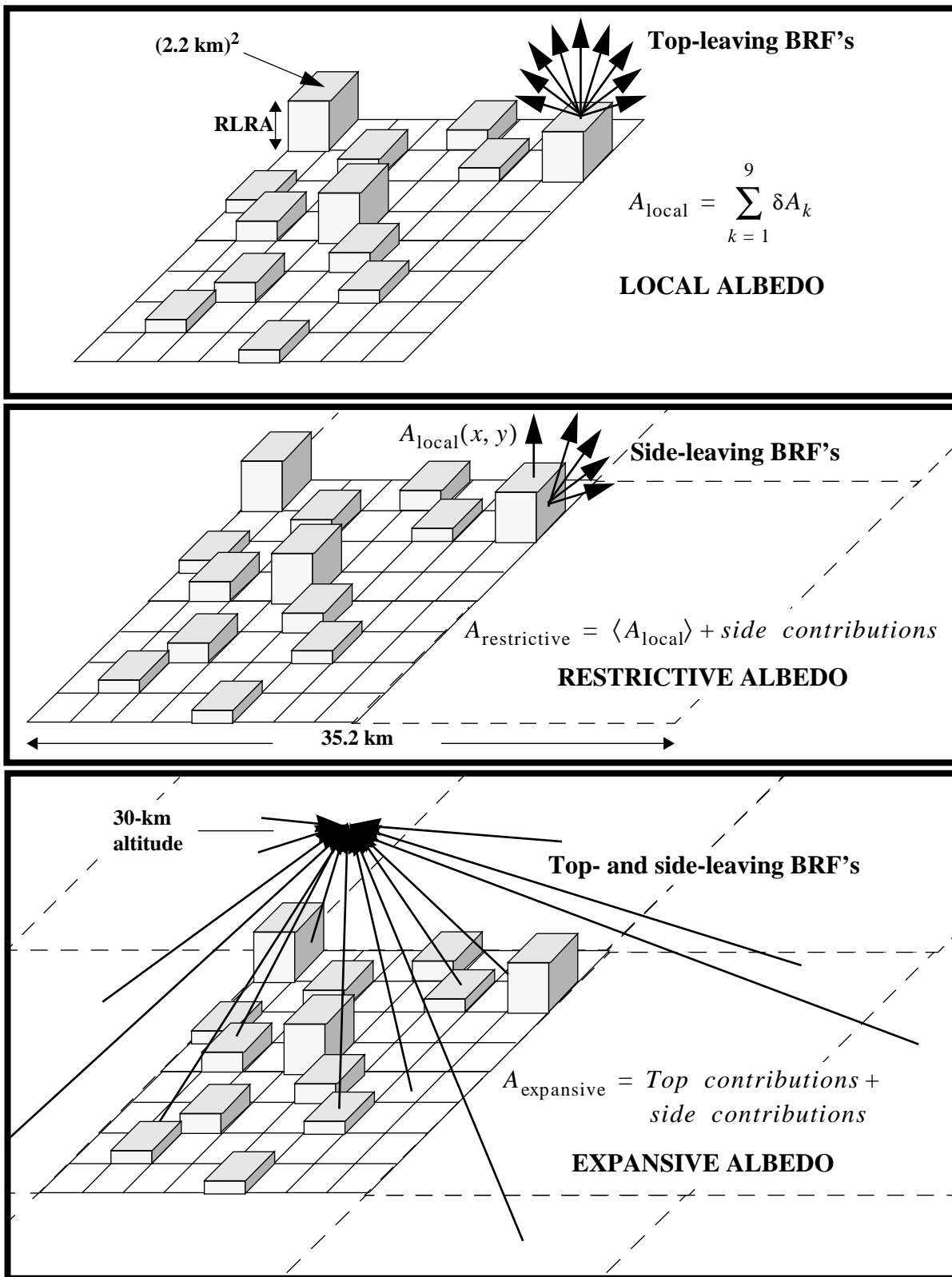
EXPANSIVE ALBEDO

Figure 1. Pictorial representations of the local, restrictive, and expansive albedos

3. ALGORITHM DESCRIPTION: DAAC PROCESSING

3.1 PROCESSING OUTLINE

Prior to the determination of albedos, several DAAC processing steps must occur. These include:

(1) Conversion of calibrated, georectified, and registered radiances from Level 1B2 to bi-directional reflectance factors (BRF's),

(2) Determination of RLRA's, and

(3) Projection of BRF's to the reflecting level.

These occur during "Stage 1" and "Stage 2" of TOA/cloud processing. The algorithm theoretical basis and associated implementation details are presented in a companion ATB *[M-8]*. In "Stage 3", regional scene classification occurs; this is also described in *[M-8]*. The subsequent routine in-flight standard processing at the DAAC to carry out the MISR top-of-atmosphere albedo retrievals is known as "Stage 4" and is described herein. Stage 4 consists of these steps:

(4a) Pre-processing to establish solid angle bin orientations and fill in missing data.

(4b) Subregion classification in support of retrieval of local albedos.

(4c) Calculation of local albedos at 2.2 km resolution, referenced to the RLRA.

(4d) Calculation of restrictive albedos at 35.2 km resolution.

(4e) Calculation of expansive albedos at 35.2 km resolution, referenced to 30-km altitude.

Processing flow concepts are shown diagrammatically in this document. The convention for the various elements displayed in these diagrams is shown in Figure 2.
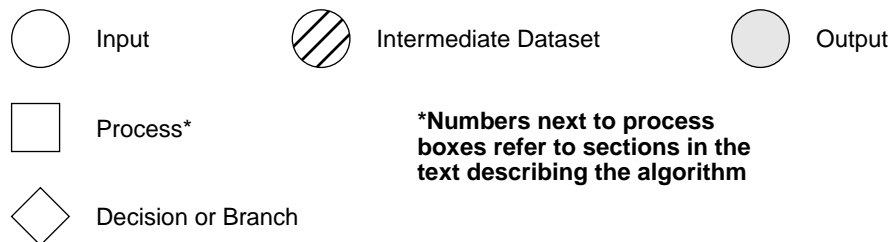
Figure 2. Conventions used in processing flow diagrams

Diagrammatic overviews of the processing concepts for generation of albedos are presented in Figures 3 - 6. Pre-processing is shown in Figure 3, subregion classification for local albedo in Figure 4, retrieval of local albedo in Figure 5, and generation of restrictive and expansive albedos in Figure 6. The processing concept for calculation of the expansive albedo classifiers is shown in Figure 7.

Numbers next to process boxes refer to sections in the text describing the algorithm

Level 1B2 Geometric Parameters

Establish boundaries of solid angle bins — 3.3.1

Solid Angle Bin Boundaries

AZM Dataset

TOA BRF's at RLRA (Tops)

Fill in missing top-leaving BRF's — 3.3.2

Filled-in TOA BRF's at RLRA (Tops)

Number of Unobscured Pixels at RLRA (Tops)

Repeat for each spectral band

TOA BRF's at RLRA (Sides)

Fill in missing side-leaving BRF's — 3.3.3

Filled-in TOA BRF's at RLRA (Sides)

Number of Unobscured Pixels at RLRA (Sides)

Repeat for each spectral band

Figure 3. Conceptual overview for albedo pre-processing

13
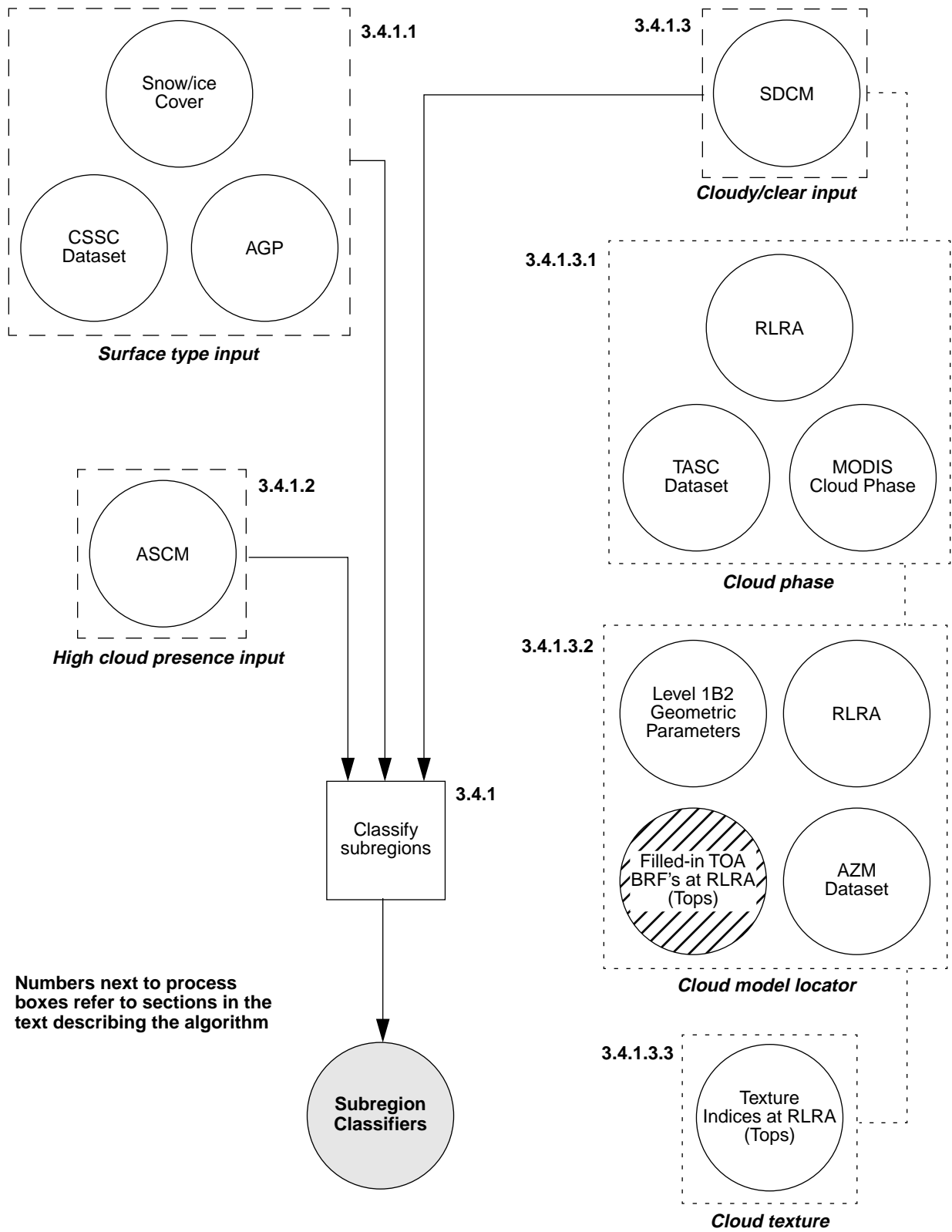
Figure 4. Conceptual overview for local albedo subregion classification

RLRA

Filled-in TOA BRF's at RLRA (Tops)

Solid Angle Bin Boundaries

Level 1B2 Geometric Parameters

AZM Dataset

TOA BRF's at RLRA (Tops)

Calculate albedo contributions from each solid-angle bin   **3.4.2**

Subregion Classifiers

Number of Unobscured Pixels at RLRA (Tops)

Local Albedo Contributions

ARP

Numbers next to process boxes refer to sections in the text describing the algorithm

3.4.3

Calculate local albedo

Repeat for each spectral band

Local TOA Albedo

Figure 5. Conceptual processing overview for local albedo retrieval

15
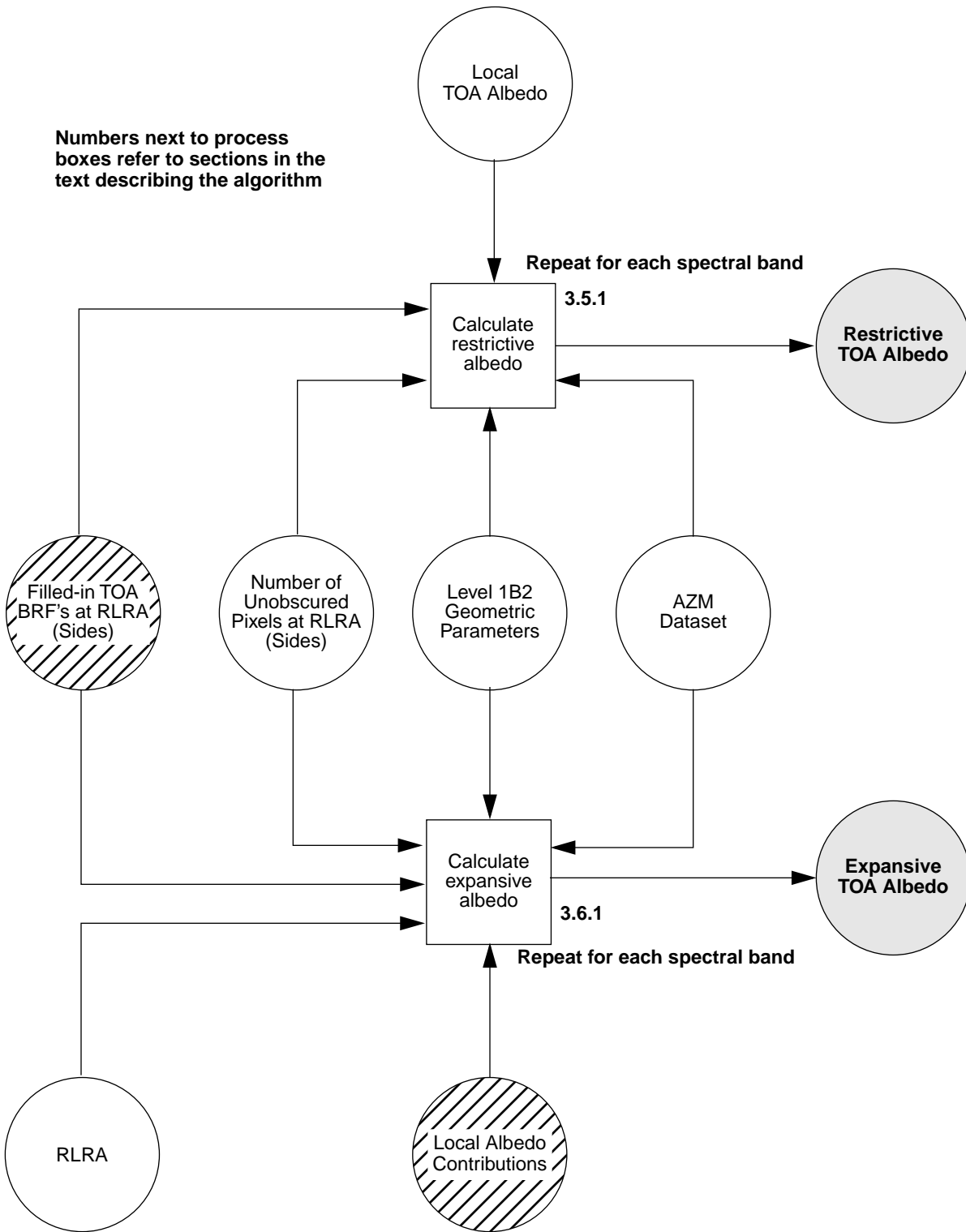
Figure 6. Conceptual processing overview for calculating restrictive and expansive albedos

16

Feature-
projected
snow/ice
cover

Feature-
projected
RCCM

SDCM

ASCM

Calculate
expansive
albedo
classifiers

3.6.2

**Expansive
TOA Albedo
Classifiers**

**Numbers next to process
boxes refer to sections in the
text describing the algorithm**
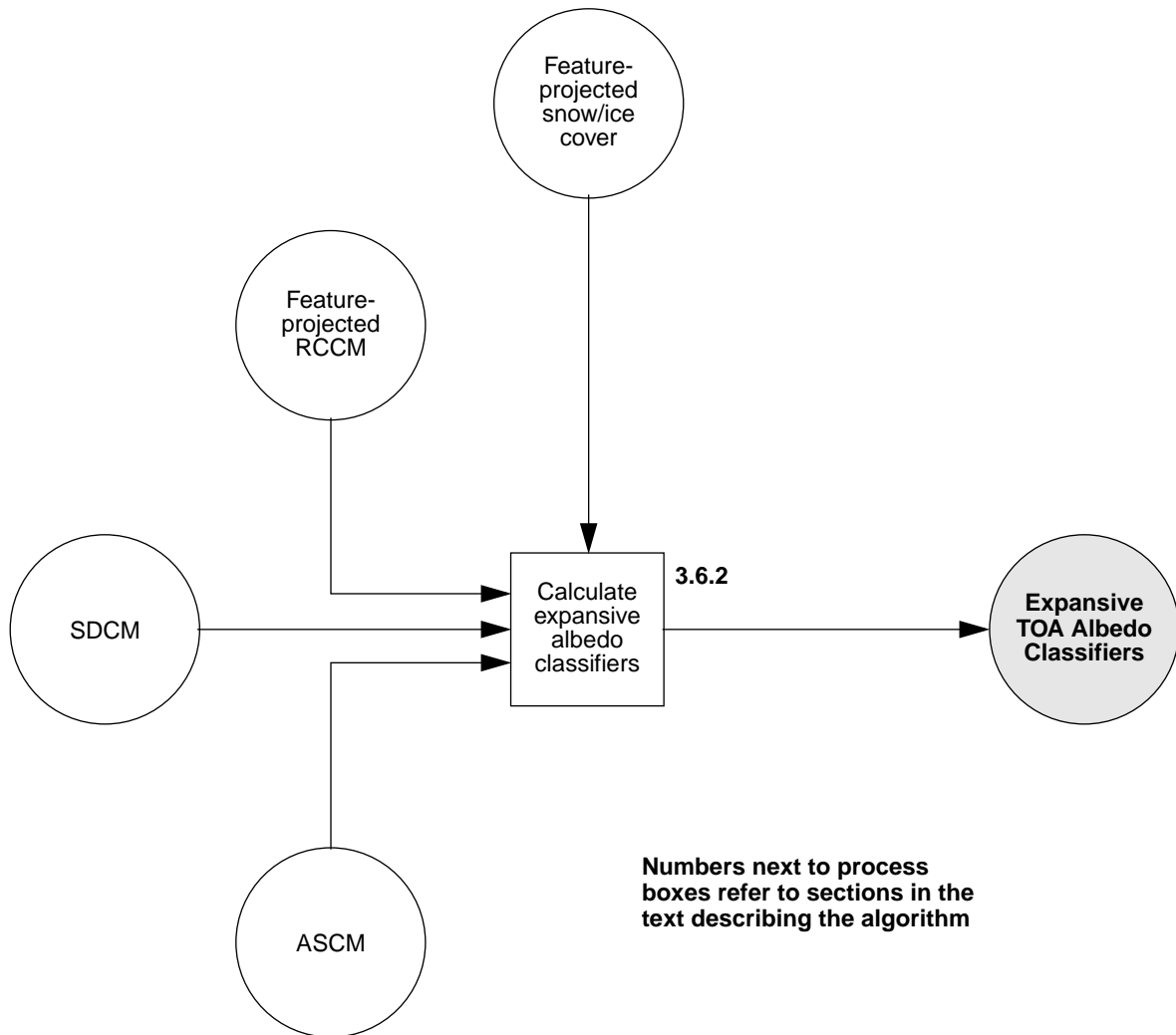
Figure 7. Conceptual processing overview for calculating the expansive albedo classifiers

17

3.2 ALGORITHM INPUT

The required inputs for TOA albedo retrieval at the DAAC come from MISR and non-MISR sources and are summarized individually in the following paragraphs. The MISR data either come directly from the MISR processing stream, or consist of relatively static inputs, generated pre-flight by the Science Team. The latter may be updated based on MISR data acquired during the course of the mission.

3.2.1 MISR data

Required inputs for the TOA albedo retrieval to be obtained from the MISR instrument or from the MISR team are summarized in Table 2. Further information on each of the inputs is provided below.

Table 2: Inputs Required for Albedo Retrieval (MISR Data)

Input data	Source of data	Reference
Ellipsoid-referenced geometric parameters	Level 1B2 Georectified Radiance Product	*[M-3]*
Reflecting Level Reference Altitude (RLRA)	Level 2 TOA/Cloud Product cloud classification processing	*[M-8]*
TOA BRF's projected to the tops and sides of RLRA columns	Level 2 TOA/Cloud Product cloud classification processing	*[M-8]*
Numbers of unobscured pixels on the tops and sides of RLRA columns	Level 2 TOA/Cloud Product cloud classification processing	*[M-8]*
Texture indices at the tops of RLRA columns	Level 2 TOA/Cloud Product cloud classification processing	*[M-8]*
Stereoscopically-Derived Cloud Mask (SDCM)	Level 2 TOA/Cloud Product cloud classification processing	*[M-8]*
Angular Signature Cloud Mask (ASCM)	Level 2 TOA/Cloud Product cloud classification processing	*[M-8]*
Feature-projected snow/ice mask	Level 2 TOA/Cloud Product cloud classification processing	*[M-8]*
Instrument radiometric uncertainties	Ancillary Radiometric Product	*[M-5]*
Land/water mask identifier	Ancillary Geographic Product	*[M-6]*
Latitude, longitude	Ancillary Geographic Product	*[M-7]*
Land surface classifier	Cloud Screening Surface Classification Dataset	*[M-4]*
Azimuthal model coefficients	AZM Dataset	*This document*
Solid angle weights and zenith angle bin boundaries	AZM Dataset	*This document*

18

3.2.1.1 Ellipsoid-referenced geometric parameters

These include illumination and view zenith and azimuth angles relative to the surface normal of the World Geodetic System 1984 (WGS84) reference ellipsoid. Azimuth angles are referenced to local North. These inputs are obtained from the Level 1B2 Georectified Radiance Product, and are provided on 17.6-km centers.

3.2.1.2 RLRA

The RLRA is retrieved stereoscopically in the earlier stages of TOA/cloud processing. It is reported on 2.2 km centers.

3.2.1.3 TOA BRF's projected to the tops and sides of RLRA columns

The RLRA is used to effect the multi-angle registration of MISR data at the height of the reflecting level. BRF's are projected to the RLRA column tops and sides during the earlier stages of TOA/cloud processing.

3.2.1.4 Numbers of unobscured pixels on the tops and sides of RLRA columns

In conjunction with projection of BRF's to the RLRA column tops and sides during the earlier stages of TOA/cloud processing, the numbers of unobscured pixels (at 275-m sampling) with which a particular camera views the top or side of an RLRA column are determined. These data provide an areal view factor which is incorporated into the albedo calculations.

3.2.1.5 Texture indices at the tops of RLRA columns

Three texture indices are calculated during earlier TOA/cloud processing from the 275-m red band BRF's projected to the tops of the RLRA columns. The first of these indices is defined to be the standard deviation of the BRF's divided by their mean value. This index is used as input to subregion classification, to establish whether the homogeneity of the subregion is appropriate for the use of plane-parallel cloud models in the calculation of local albedo.

3.2.1.6 Stereoscopically-Derived Cloud Mask (SDCM)

The SDCM is retrieved as part of Level 2 cloud detection and classification. It is provided on 1.1-km centers, and classifies $(1.1\text{-km})^2$ subregions as Cloud with High Confidence (CloudHC), Cloud with Low Confidence (Cloud LC), Near Surface, Clear, or No Retrieval (NR). It is determined using stereoscopic and radiometric cloud detection methodologies. It is used to establish whether the clear or cloudy sky albedo retrieval methodology should be implemented.

3.2.1.7　Angular Signature Cloud Mask (ASCM)

The ASCM uses the Band-Differenced Angular Signature method *[6]* to detect the presence of high (e.g., cirrus) cloud. The mask is provided on 1.1-km centers, and classifies (1.1-km)^2 sub-regions as CloudHC, CloudLC, Clear with Low Confidence (ClearLC), Clear with High Confidence (ClearHC) or No Retrieval. It is used to establish the amount of Rayleigh scattering that should be factored into the albedo retrieval algorithm.

3.2.1.8　Feature-projected snow/ice mask

This is used in selecting the appropriate cloud models from the AZM Dataset. Input from MODIS, the National Snow and Ice Data Center (NSIDC), or the Data Assimilation Office (DAO) are used, if available, to establish a snow/ice mask; otherwise, climatological data are obtained from the MISR Terrestrial Atmosphere and Surface Climatology (TASC) Dataset *[M-11]*. This mask is then projected to the SOM location of cloud and surface features.

3.2.1.9　Instrument radiometric uncertainties

These data are used in establishing criteria for determining the goodness of model fits to the data. They are obtained from the MISR Ancillary Radiometric Product (ARP). Information on how the data are derived is presented in *[M-5]*.

3.2.1.10　Land/water mask

This is a land/ocean/inland water/ephemeral water/coastline mask obtained from the MISR Ancillary Geographic Product (AGP). The data are provided on 1.1-km centers. The AGP is generated at the MISR SCF and stored at the DAAC. Further details of the AGP are provided in *[M-6]*.

3.2.1.11　Latitude/longitude

The AGP contains the latitude and longitude for each 1.1 km grid-center on the surface ellipsoid.

3.2.1.12　Land surface classifier

Choosing the Azimuthal Model for cloudy scenes requires determining whether the surface is vegetated or non-vegetated. The Cloud Screening Surface Classification (CSSC) Dataset is used for this purpose. It contains 1580 surface types, each of which has additional indicators specifying whether the surface is classified as desert or non-desert and as vegetated or non-vegetated. The latter is used during TOA albedo calculation. Generation of the CSSC Dataset is described in *[M-4]*.

3.2.1.13 Azimuthal model coefficients

Azimuthal models, or AZM's, are used to integrate BRF's over angle to derive spectral albedos. For cloudy scenes, these consist of sets of coefficients, categorized by scene type, that constitute predetermined look-up tables contained within the AZM Dataset. The AZM coefficients depend on view and illumination geometry and cloud and surface types. Scene identification data are used during routine processing to select the appropriate AZM (in particular, the corresponding coefficients) to facilitate the angular integrations. The AZM Dataset is generated at the MISR SCF prior to launch and delivered to the DAAC (see Chapter 4). For clear scenes, a parametric azimuthal model is used, and look-up table input is not required.

3.2.1.14 Solid angle weights and zenith angle bin boundaries

When the modeling approaches do not meet certain criteria, solid angle weighting is used for retrieving local albedos. A form of solid angle weighting is also used for side-leaving BRF contributions to restrictive and expansive albedos. No scene-type dependent modeling is attempted for side-leaving contributions, because the most typical case of large RLRA column sides is at the border separating cloudy and clear pixels, and in such cases some of the side-leaving radiation originates from the cloud sides, and the rest, from the underlying surface. Scene-type dependent modeling would be highly uncertain due to this mixing and because overlying clouds modify the illumination (and hence the reflection) of the underlying surface. The solid angle weighting coefficients are stored in the AZM Dataset. In addition, the boundaries of the solid angle bins for which the weighting coefficients are defined, in the direction of cosine of the view zenith angle, are pre-established. The locations of these bin boundaries are also stored in the AZM Dataset, and used during clear-sky albedo retrievals.

3.2.2 Non-MISR data

Inputs for the TOA/cloud retrievals to be obtained from non-MISR sources are summarized in Table 3. The MODIS input is not expected to be used at launch; however, it will be integrated into the processing stream post-launch, once its influence can be evaluated.

Table 3: Inputs Required for Albedo Retrieval (Non-MISR Data)

Input data	Source of data
Cloud phase identifier	MODIS Level 2 or TASC Dataset
Snow cover and sea ice extent	MODIS Level 2, NSIDC, DAO, or TASC Dataset

3.2.2.1 Cloud phase identifier

After launch, information from MODIS about the phase of the cloud particles (liquid, ice, or

mixed) are expected to be used to improve the choice of AZM for albedo calculations. In the event that these data are unavailable, default values based on RLRA and climatological temperature profiles contained in the TASC Dataset will be used.

3.2.3 Snow cover and sea ice extent

This is used in the surface classification section of the albedo processing, to determine whether the surface is snow or ice covered in order to retrieve the correct coefficients from the AZM Dataset. The current assumption is that NSIDC input, using passive microwave data, will be used, to eventually be superseded by MODIS snow cover and sea ice retrievals. If neither NSIDC nor MODIS data is available, Data Assimilation Office (DAO) data based on NOAA retrievals are used. If none of these sources are available, TASC climatological data are used as the default.

Depending on the source of snow/ice data, the input may be in the form of a mask (Snow Covered/Not Snow Covered and Ice Covered/Not Ice Covered) or in the form of snow equivalent depths and sea ice fraction.

3.3 THEORETICAL DESCRIPTION: PRE-PROCESSING

The albedo retrieval methods described in this ATB make use of precalculated weighting coefficients which are stored in the Azimuthal Model (AZM) Dataset. These precalculated weights correspond to the solid angle bins in an "igloo" configuration (see §3.3.1). The boundaries of these bins depend on cosine of viewing zenith angle. Because view angle can vary somewhat across the field-of-view of an individual camera, the establishment of precalculated weights requires the use of nominal values for the view angle cosines. These nominal values are denoted by the variable μ, where μ_k is the nominal view angle cosine for the kth camera, and k varies from $k = 1$ for Df to $k = 9$ for Da. The nominal values of μ_k are contained in the AZM Dataset and provided in §4.1. Then, each bin is centered in μ-space on the nominal cosine of the respective camera zenith angle. The azimuthal limits are from 0 to 2π for bin 5 (nadir), and $\pm \pi/2$ about the mean camera azimuth for the other bins.

The actual view and solar zenith angle geometries used in albedo retrievals apply to regions measuring 17.6 km on a side, as this is the area over which camera and sun geometry are provided by the Level 1B2 geometric parameter data. Note that since the albedo retrieval involves normalization to incident flux, which depends on solar zenith angle, we avoid potential singularities at the terminator by not processing albedos for solar zenith angles greater than 87.7° ($\mu_0 < 0.04$). In addition, for any $(2.2\text{-km})^2$ subregion where all four values of the SDCM are designated No Retrieval, a value of RLRA does not exist. In these infrequent instances, local albedo is not calculated. If valid solar zenith angle data do not exist, the local and restrictive albedos for this pixel as well as the contribution of this pixel to the expansive albedo are not calculated.

3.3.1 Establish boundaries of solid angle bins

The upwelling irradiance contributing to the local albedo is considered to be the sum of 9 components that account for the total reflected irradiance into each of 9 solid angle bins, one for each camera direction. That is,

$$A_{\text{local}} = \sum_{k=1}^{9} \delta A_k \tag{1}$$

The distribution of solid angle bins within which the values δA_k are defined is given by the "igloo" configuration, shown in Figure 8.

Side view   **Top view**
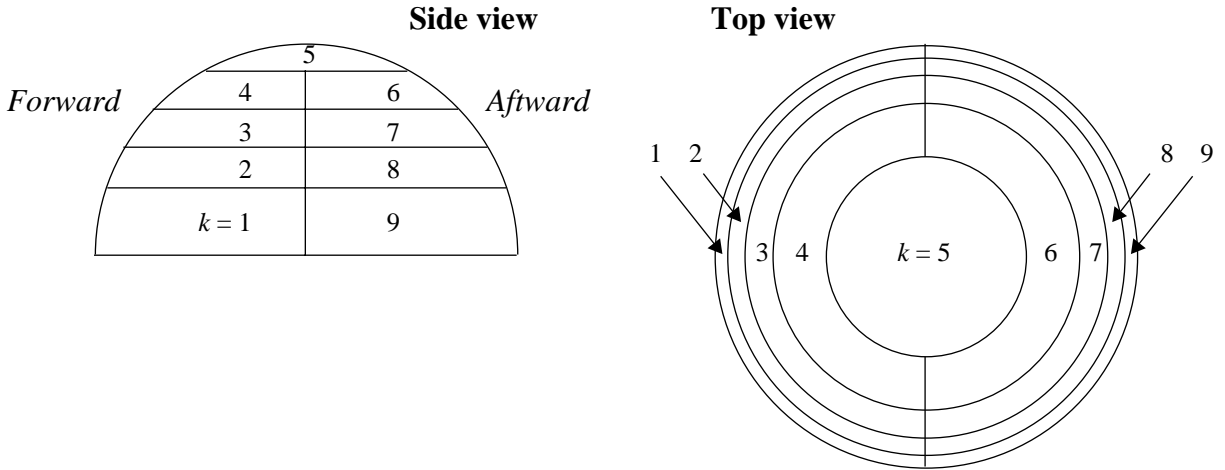
Figure 8. Depiction of solid angle bins in the "igloo" configuration

Each δA_k is based primarily on the corresponding average BRF on the top of the RLRA column, $\overline{B}_k$ (where the averaging is performed over all valid unobscured pixels at the 275-m level; see *[M-8]*), but is modified to allow for zenith angle variation. It may also be corrected to account for a dependence on the relative azimuthal angle. The degree of azimuthal modification will generally depend on the index k, and the solar zenith angle. For example, for overhead Sun, or for $k = 5$ (the An camera), no azimuthal modification is required.

The values of zenith angle cosine which define the boundaries of the solid angle bins are obtained from the AZM Dataset. They are based on nominal camera zenith angle cosines because they are used in creating the contents of the AZM Dataset (see §4.4.1). The orientation of the "igloo" in azimuth angle is optimized to place the camera boresights as close as possible to the center of their respective bins. Since the view azimuths change significantly across the width of the swath

and from pole to pole, the azimuthal orientation of the "igloo" is therefore determined during the albedo retrieval processing. During DAAC processing, the solid angle bin boundaries are used explicitly in the integration of the clear-sky parametric AZM.

Letting ϕ_k be the view azimuth of the kth camera, the values of view azimuth which define the limits of the solid angle bins are determined as follows:

(1) Based on the relative azimuth angle of the D camera which measures forward scattering, and on the solar zenith angle, choose a mean azimuth angle. The mean azimuth values are stored in the AZM dataset.

$$\text{Equation deleted} \tag{2}$$

(2) For $1 \leq k \leq 4$, the azimuth limits are $\left(\phi_{mean} - \frac{\pi}{2} \right)$ to $\left(\phi_{mean} + \frac{\pi}{2} \right)$.

(3) For $6 \leq k \leq 9$, the azimuth limits are $\left(\phi_{mean} + \frac{\pi}{2} \right)$ to $\left(\phi_{mean} + \frac{3\pi}{2} \right)$.

(4) For $k = 5$, the azimuth limits are ϕ_{mean} to $(\phi_{mean} + 2\pi)$.

3.3.2 Fill in missing top-leaving BRF's

Should one or more values of $\overline{B}_k$ be missing, such that there are less than 9 values (but at least one), the following methodology is used in each spectral band for filling in the missing data using interpolated or extrapolated values of $\overline{B}$. Note that a missing top-leaving BRF means that radiometric data are not available at a particular value of k (e.g., due to a CCD failure), yet the number of unobscured pixels on the RLRA top, t_k (see *[M-8]*), which is determined from geometric considerations, is > 0. Instances in which $t_k = 0$ do not constitute missing data according to this definition. However, for any camera for which $t_k = 0$, the corresponding BRF is set to 0.0 to reflect the fact that a top BRF could not have been measured. In those instances in which any camera has a missing unobscured pixel count on the RLRA top, BRF values are not filled in for any camera and the local albedo cannot be computed for this RLRA top.

(1) For each l, where l signifies a camera angle at which a top-leaving BRF is missing, identify k_{low} and k_{high}, the nearest camera angles with available data and $t_k > 0$, where k_{low} $< l$ and $k_{high} > l$. However, if $l - k_{low} > \Delta k_{top}$, drop k_{low} from consideration, and if k_{high} $- l > \Delta k_{top}$, drop k_{high} from consideration. We set $\Delta k_{top} = 8$, which causes there to be no limit on how far away the cameras providing the data can be from the angle to be filled in. Depending on the location of l (e.g., $l = 1$ or $l = 9$), and the amount of available data, only k_{low} or k_{high} may be identifiable.

(2) If neither k_{low} nor k_{high} is identified, no value is filled in for $\overline{B}_l$, and it is still considered missing.

(3) Set

$$\overline{B}_l = \overline{B_{k_{low}}} \qquad \text{if only } k_{low} \text{ is identified} \tag{3}$$

(4) Set

$$\overline{B}_l = \overline{B_{k_{high}}} \qquad \text{if only } k_{high} \text{ is identified} \tag{4}$$

(5) Set

$$\overline{B}_l = \frac{(k_{high} - l)\overline{B_{k_{low}}} + (l - k_{low})\overline{B_{k_{high}}}}{k_{high} - k_{low}} \qquad \text{if both } k_{low} \text{ and } k_{high} \text{ are identified} \tag{5}$$

The above procedure is applied to each value of l independently. Thus, k_{low} and k_{high} are based only on the presence of original data, that is, k_{low} and k_{high} cannot correspond to locations which were themselves filled in.

Note that the weights used in calculating local albedos are not based on the individual values of $\overline{B}_k$, just the angles and obscuration factors, so these are unaffected by missing values of $\overline{B}_k$. However, the resulting albedos are flagged accordingly to note they are based on incomplete measurements. In the case where only a single $\overline{B}_k$ is available, the above procedure will set the BRF at all other angles to this value. Determination of albedos will then be feasible, but the associated quality assessment flags will imply reduced confidence in the accuracy of the result. If there are no $\overline{B}_k$ available, then local albedo is not calculated.

3.3.3   Fill in missing side-leaving BRF's

The approach for filling in missing data described in §3.3.2 is also applied to the set of average BRF's assigned to the sides of the RLRA columns, $\overline{B_{\text{sides}, k}}$. Side-leaving BRF's are not required for local albedo, but are used in the restrictive and expansive albedo calculations. Unlike the $\overline{B}_k$ values, which are registered to the RLRA tops, and therefore correspond to the same local scene, the $\overline{B}_{\text{sides}, k}$ assigned to a given RLRA column may come from different geographic locations (e.g., if they correspond to views underneath a cloud and therefore intersect different surface points). Thus, we do not necessarily expect continuity in $\overline{B}_{\text{sides}, k}$ from one angle to the next, as we would expect for $\overline{B}_k$. Consequently, the procedure for filling in side-leaving BRF's is similar to the approach in §3.3.2 except we set a more restrictive limit on how far away a particular angle that is providing data can be from the angle to be filled in. Note that a missing side-leaving BRF means

that radiometric data are not available at a particular value of k, yet the number of unobscured pixels on the RLRA side, s_k (see *[M-8]*), is > 0. Instances in which $s_k = 0$ do not constitute missing data according to this definition.

The following procedure is followed for each spectral band:

(1) Identify k_{low} and k_{high} as in step (1) of §3.3.2, where k_{low} and k_{high} correspond to locations with available data where $s_k > 0$. However, if $l - k_{low} > \Delta k_{side}$, drop k_{low} from consideration, and if $k_{high} - l > \Delta k_{side}$, drop k_{high} from consideration. We set $\Delta k_{side} = 1$.

(2) If neither k_{low} nor k_{high} is identified, no value is filled in for $\overline{B_{sides,\,l}}$, and it is still considered missing. Solid angle renormalization will be used to compensate for this during the calculation of restrictive and expansive albedos.

(3) - (5). Otherwise, an analogous procedure to steps (3) - (5) of §3.3.2 is followed. Again, the procedure is applied to each value of l independently.

3.4   THEORETICAL DESCRIPTION: LOCAL ALBEDO

3.4.1   Classify subregion

3.4.1.1   Surface type

All subregions are classified according to surface type. One of four designations is selected: Snow/Ice, Water, Vegetated Land, or Non-vegetated Land. The following procedure is used:

(1) *Snow or ice*. If the snow/ice mask indicates the presence of snow or ice for any of the four $(1.1\text{-km})^2$ subregions within the $(2.2\text{-km})^2$ subregion, this designation is selected.

(2) *Water*. If all $(1.1\text{-km})^2$ subregions within the $(2.2\text{-km})^2$ subregion are classified by the Ancillary Geographic Product as ocean or inland water, and the subregion is not snow or ice covered, this designation is selected.

(3) *Vegetated* or *non-vegetated land*. For all subregions that do not have either the snow/ice or water designation, interrogate the CSSC Dataset (see *[M-4]*) at the location corresponding to the center of the $(2.2\text{-km})^2$ subregion to establish whether the surface should be classified as vegetated or non-vegetated. The latitude and longitude for indexing the CSSC Dataset are determined by averaging the values, obtained from the AGP, from the four $(1.1\text{-km})^2$ subregions which comprise the $(2.2\text{-km})^2$ subregion.

3.4.1.2   High cloud presence

All subregions are classified according to whether or not the presence of high (cirrus) clouds

is identified. The Angular Signature Cloud Mask (ASCM) is used to classify each subregion as High Cloud Present, High Cloud Not Present, or High Cloud Undetermined.

(1) If any of the ASCM designations within the (2.2-km)^2 subregion indicates the presence of high cloud (i.e., is designated CloudHC or CloudLC), the classification High Cloud Present is chosen.

(2) If none of the ASCM designations are CloudHC or CloudLC, the classification High Cloud Not Present is chosen.

(3) The one exception to step (2) is if all four designations are No Retrieval (NR). In this case the classification High Cloud Undetermined is chosen.

3.4.1.3   Cloudy vs. clear methodology

Different techniques are used for calculating the local albedo, depending on whether the (2.2-km)^2 subregion is established to be cloudy or clear. The SDCM, which is provided on 1.1-km centers, is used to establish this, according to the following logic:

(1) If all four SDCM values within the subregion are classified as Clear, the subregion is designated AZM Clear, meaning that the clear sky methodology is to be used.

(2) If any of the SDCM values within the subregion are classified as CloudHC or CloudLC, the subregion is designated AZM Cloud, meaning that the cloudy sky methodology is to be used.

(3) In all other cases, it is not possible to decide whether the subregion should be processed using the cloudy or clear methodology. This can occur, for example, when all four SDCM values are designated No Retrieval, or some are designated No Retrieval and some are Clear. In these instances, the Solid Angle Weighting method, which is common to both clear and cloudy scenes, is used, and the subregion is designated AZM Undetermined.

If the subregion is classified as AZM Cloud, then further classification is performed as follows.

3.4.1.3.1   *Cloud phase*

For subregions classified as AZM Cloud, we also designate the cloud phase. In later phases of the MISR mission, MODIS cloud phase will be used for this purpose. Until then, the RLRA and the temperature profile vs. height contained in the TASC Dataset are used to establish a cloud-top temperature using linear interpolation. If $T_{cloud} > 0°C$, the cloud phase is set to Liquid. If $T_{cloud} < -43°C$, the cloud phase is set to Ice. Otherwise, it is set to Unknown.

3.4.1.3.2 Model locator indices

Local albedo determination using cloud models for cloudy subregions makes use of information in the AZM dataset, stored according to several index numbers. Identifying these index numbers at this stage of the processing is a preparatory step for local albedo retrieval. The set of index numbers is chosen to take advantage of the information that will routinely be available on the scene properties having the largest influence on cloud reflection. The index numbers provide information on solar and viewing geometry, the underlying surface, cloud phase, cloud brightness (related to optical thickness), and the amount of Rayleigh scattering. Additionally, the subregion texture is used to test the appropriateness of the "Deterministic" retrieval pathway; i.e., to determine whether spatial variations in cloud reflection allow the use of homogeneous cloud models. Specifically, the following index numbers are established:

(1) i_{sun}, the index number corresponding to the bin within which the solar zenith angle falls. The Level 1B2 ellipsoid-referenced geometric parameters are used as input. A sufficient number of solar zenith angle bins is included in the AZM Dataset such that interpolation of the AZM coefficients over this variable is not required.

(2) $i_{view\_zenith\_angle}(k)$, the index number corresponding to the bin within which the view zenith angle of the cameras fall, where k represents the camera identifier. The Level 1B2 ellipsoid-referenced geometric parameters are used as input, and no interpolation is required.

(3) $i_{azim}(k)$, the index numbers corresponding to the bins within which the relative view-sun azimuth angles fall for camera k, where $k =$1, 2,..., 9. The Level 1B2 ellipsoid-referenced geometric parameters are used as input to establish the bin into which the relative azimuth falls as well as the distance to the neighboring bin, and linear interpolation of the AZM coefficients to the azimuth angle of the observations is used. The azimuth binning depends on the solar zenith angle.

(4) $i_{igloo}(k)$, the index numbers determining whether the forward cameras are observing predominantly forward or backward scattered light, and whether the aftward cameras are observing predominantly backward or forward scattered light. This is needed to establish the proper orientation of the "igloo" shown in Figure 8. The geometry of the Df camera is used for this purpose if valid angular data is available. If this is not the case, the Da camera is used if it has valid data. For the forward cameras, $i_{igloo}(k)$ is set to forward scattering if the relative azimuth of the Df camera is $\leq 90°$ or $> 270°$, or if the relative azimuth of the Da camera is $> 90°$ and $\leq 270°$.; otherwise it is set to backward scattering. For the aftward cameras, $i_{igloo}(k)$ is set to the value opposite to that of the forward cameras. No designation is necessary for An because the value of δA_5 is always estimated using the Solid Angle Weighting methodology which does not require the use of this index. If neither the Df nor the Da camera contain valid angular data, the $i_{igloo}(k)$ index number cannot be calculated and solid-angle weighting must be used to calculate the local albedo.

(5) i_{surf}, the index corresponding to the appropriate surface scene type (see §3.4.1.1). If the land-water mask indicates land at the appropriate pixel yet the CSSC indicates water, a nearest neighbor search is performed to find the closest pixel in the CSSC that has a land classification. If the search fails to find a land classification within the given radius (currently 1 CSSC pixel) a default (vegetated) land class is used instead.

(6) i_{phase}, the index number corresponding to the cloud phase (see §3.4.1.3.1). The probability of liquid water in the cloud is determined by comparing T_{cloud} to thresholds from the AZM Dataset. For Unknown cloud phase, linear interpolation between the AZM coefficients for Liquid and Ice is performed, as described in §3.4.2.1.1 and §3.4.2.1.2.

(6) $i_{alt}(band\ 1)$ and $i_{alt}(band\ 2)$, separate index numbers for bands 1 and 2, based upon the value of the RLRA of the subregion, where the range of index numbers depends upon the identity of the band. These index numbers are important for taking into account the magnitude of Rayleigh scattering that occurs above the main reflecting layer.

(7) $i_{bright}(k)$, the index numbers corresponding to the brightness of the red-band top-leaving BRF's for the particular camera under consideration, obtained by comparing the BRF to a series of thresholds, ξ_{bright}, from the AZM Dataset. These thresholds are functions of the indices i_{sun}, $i_{view\_zenith\_angle}(k)$, $i_{azim}(k)$, i_{surf}, and i_{phase}, and the camera identifier k. Note that wherever we calculate the brightness index number for a given camera k, all of the model locators for the brightness are also determined for the same camera k. For Unknown cloud phase, the thresholds ξ_{bright} are determined from a linear interpolation of the thresholds for ice and liquid phases. The interpolation is based on the probability of these two cloud phases, determined from the AZM dataset as a function of T_{cloud}. No interpolation of the AZM coefficients in cloud brightness is required, however.

3.4.1.3.3 Texture

If the subregion is classified as AZM Cloud, we establish a texture classification as Homogeneous, Heterogeneous, or Texture Not Available. The following algorithm is used to do this. First, we select the "homogeneity reference" camera by checking if the red band BRF at the top of the RLRA, texture index ζ (defined as the standard deviation/mean; see *[M-8]*) and angular data are available for the An camera. An available BRF refers to original (i.e., not filled in) data. If not, calculate the scattering angles of the Af and Aa cameras, and choose the one with the smaller scattering angle (i.e., closer to forward scattering) for which the red band BRF, texture index and angular data are all available. If this is unsuccessful, repeat the same sequence for the B cameras. If this still fails to identify the homogeneity reference camera, the texture is classified as Texture Not Available. No texture classification is possible if the solar zenith angle does not contain valid data. The scattering angle, Ω, is calculated from

29

$$\cos\Omega = -\mu\mu_0 + (1 - \mu^2)^{\frac{1}{2}} \cdot (1 - \mu_0^2)^{\frac{1}{2}} \cdot \cos(\phi - \phi_0) \tag{6}$$

where μ is the cosine of the view zenith angle, μ_0 is the cosine of the solar zenith angle, and ϕ - ϕ_0 is the relative view-sun azimuth angle.

If the homogeneity reference camera (HRC) has been identified, we now establish whether the cloud is to be classified as Homogeneous or Heterogeneous. Letting k_{HRC} denote the camera identifier of the homogeneity reference camera, this is done as follows:

(1) Compare the HRC texture index ζ to a threshold ξ_{text}, that is, check whether $\zeta \leq \xi_{text}$, where ξ_{text} is a function of i_{sun}, $i_{view\_zenith\_angle}(k_{HRC})$, $i_{azim}(k_{HRC})$, and $i_{bright}(k_{HRC})$. ξ_{text} is obtained from the AZM Dataset.

(2) If $\zeta \leq \xi_{text}$, classify the subregion as Homogeneous. Otherwise, classify it as Heterogeneous.

3.4.2 Calculate albedo contributions from each solid angle bin

For subregions classified as AZM Cloud the cloudy sky methodology described in §3.4.2.1 is attempted and for those classified as AZM Clear the clear sky methodology described in §3.4.2.2 is attempted. For any camera angle and band at which the cloudy or clear sky methodology does not meet certain established criteria, the Solid Angle Weighting methodology of §3.4.2.3 is followed for that camera and band. For subregions classified as AZM Undetermined, we default to the Solid Angle Weighting methodology of §3.4.2.3 for all cameras and bands.

For each $(2.2\text{-km})^2$ subregion, local albedos are calculated on a band-by-band basis. That is, the steps outlined below are performed for each spectral band independently.

3.4.2.1 Subregions classified as AZM Cloud

There are three techniques for determining each contribution, δA_k, to the local albedo for cloudy skies, the choice of which depends on how well the measurements match the database of modeled angular variation:

(1) If the measurements match a specific model according to an established set of criteria, the azimuthal correction is found from direct modeling (known as the Deterministic method). Due to the large variety of cloud inhomogeneities, this deterministic weighting of measured BRF values will initially be used only for homogeneous, plane-parallel cloud models.

30

(2) If the measurements fail to match a plane-parallel model, yet have an angular dependence that is consistent with generic cloud behavior, as determined by established criteria, a generic model is used to provide a statistical best guess for the azimuthal correction (known as the Stochastic method). Such a model takes into account basic cloud properties, but is not specific to any particular cloud type.

(3) If the measurements fail to satisfy the criteria required by either of the above approaches, then no azimuthal correction is made and the integration is based on zenith angle variation only (known as the Solid Angle Weighting method).

This approach appears to be the best available with pre-launch information. However, as MISR data are analyzed and compared against our pre-launch knowledge, the accuracy of the albedo retrieval techniques using the Deterministic, and especially the Stochastic method, are expected to improve. Note that for a given determination of the local albedo, it is possible for each δA_k contribution to be determined by a different method; that is, it is possible, for example, for Deterministic weighting to be used for cameras Df and Ba, Stochastic for Cf, and Solid Angle Weighting for the remainder.

Using different retrieval methods for different cameras is appropriate if detailed azimuthal modeling is required for some view angles, while solid angle weighting is sufficiently accurate for others (e.g., near-nadir directions). It can also be justified by considering that although all 9 cameras are registered to the same RLRA, it is possible that they actually measure radiation reflected from different locations. This can be the case if, for example, the 9 cameras are not co-registered correctly (due to an RLRA retrieval error or lack of RLRA-retrieval altogether). In addition, even if the RLRA is determined correctly, the concept of using a single RLRA can cause different cameras to measure reflection from different objects in the cases of multilayer cloud situations or sub-pixel variability. For example, if a thick cloud covers only half of a pixel, forward cameras registered to the top of the RLRA column can measure the reflection from the top and the side of this cloud, while the nadir and aft cameras registered to the same RLRA-top measure reflection both from the top of the cloud and from the neighboring clear region.

In general, each δA_k may depend on up to all 9 of the measured values $\overline{B}_l$, the average BRF for the lth camera, related by a choice of weights, w_{kl}, such that

$$\delta A_k = \sum_{l=1}^{9} f_{kl} \delta A_{kl} = u_k \sum_{l=1}^{9} f_{kl}(w_{kl}\overline{B}_l + \varepsilon_k) \tag{7}$$

where

u_k is the unobscured fraction, $t_k/64$, of the RLRA, given t_k unobscured 275 m pixels for the kth camera on the top of the RLRA column;

31

w_{kl} weights the contribution of the average unobscured BRF, $\overline{B}_l$, to δA_{kl};

f_{kl} is a normalizing factor that depends on the actual number of BRF's and the methodology used. The determination of f_{kl} is inherent in the following discussions of the Deterministic, Stochastic, and Solid Angle Weighting approaches;

and ε_k is included to eliminate bias error arising, for example, from the fact that the MISR cameras do not observe view angles > 70.5°. This bias term is not used in Solid Angle Weighting.

In choosing the appropriate coefficients for deterministic and stochastic modeling, the key distinction to make is not that of the "absolute camera identifier", but rather of the value of the viewing zenith angle and whether it is viewing forward or back scattering. Therefore, the same coefficients can be used for both forward and aftward cameras, and so in accessing the AZM Dataset for stochastic retrievals the actual processing software replaces the index numbers k and l (ranging from 1 to 9) by k' and l' (ranging from 1 to 5). The values of k' and l' are set to 1 for both D cameras, to 2 for both C cameras, and so on. For deterministic modeling, the datasets are accessed by the variables k' and m', where $m' = l' - k'$ in place of k and l. In using the coefficients within the albedo algorithm, however, it is necessary to refer only to the index numbers k and l and for the sake of clarity the rest of this ATB document will follow this convention.

Note that in Eq. (7), the determined δA_k values depend on measurements taken both inside and outside the solid angle bin for δA_k. Including outside measurements improves the way our calculation of δA_k accounts for cloud reflection into directions that are part of the solid angle bin, but different from the direction of the measurement within this bin. For example, the second camera (Cf, counting from the most forward-looking direction) can help in estimating δA_1 (the contribution within the solid angle bin for the Df camera) by improving the way we account for reflection into directions that fall between the two cameras' viewing directions.

3.4.2.1.1 *Deterministic method*

If $\mu_0 \leq 0.9$, we check the suitability of direct modeling to obtain the coefficients needed to evaluate Eq. (7) for each solid angle bin (excluding $k = 5$) and each (2.2-km)^2 subregion. The models are chosen based on scene classification and sun-view geometry as determined in §3.4.1.

If the subregion texture is classified as Heterogeneous, we do not attempt Deterministic modeling at any camera angle, and proceed directly to Stochastic modeling. If the texture is classified as Homogeneous or Texture Not Available, the following steps are performed for each camera angle. That is, we determine all values of k, other than nadir, at which Deterministic modeling is suc-

cessful before proceeding, if necessary, to Stochastic modeling. Deterministic modeling is not possible if the BRF is filled-in or totally obscured, or if any angular data are missing. The Deterministic modeling methodology proceeds as described in the following paragraphs.

Letting i_{band} be the spectral band identifier, we find the values of w_{kl} and ε_k for the appropriate deterministic model in the AZM Dataset that corresponds to the conditions which have thus far been established [i_{sun}, $i_{view\_zenith\_angle}(l)$, $i_{azim}(l)$, $i_{igloo}(k)$, i_{band}, i_{surf}, i_{phase}, i_{alt}, $i_{bright}(k)$], noting that $i_{view\_zenith\_angle}$, i_{azim}, i_{igloo}, and i_{bright} depend on camera angle and i_{alt} depends on spectral band. [Note that the index numbers related to the view angle ($i_{view\_zenith\_angle}$ and i_{azim}) are for camera l, not k. This is because δA_k is estimated from the measurement of camera l, whose viewing angle index numbers are often different from those of camera k.] Next, find the values of w_{kl} and ε_k for the neighboring deterministic models for both cloud phases (liquid and ice), and $i'_{azim} = i_{azim} + 1$. Then we determine the actual w_{kl} and ε_k values through a two-dimensional linear interpolation over the relative azimuth and cloud phase (using the actual azimuth value and the probability of liquid cloud phase), while treating all other index numbers as constant. Then, we calculate the estimates of δA_{kl} given by

$$\delta A_{kl} = w_{kl}\overline{B}_l + \varepsilon_k \tag{8}$$

for

(1) $l = k$, $l = k + 1$, and $l = k - 1$ for any camera other than Df or Da;

(2) $l = k$ and $l = k + 1$ for camera Df;

(3) $l = k$ and $l = k - 1$ for camera Da.

If δA_{kk} and the other value(s) of δA_{kl} agree, that is, if

$$\left|\delta A_{kl} - \delta A_{kk}\right| \leq \Delta_d \tag{9}$$

for all relevant values of l then the search for a deterministic model is considered successful. The values of Δ_d are stored in the AZM Dataset and indexed by i_{sun}, $i_{azim}(l)$, $i_{igloo}(k)$, $i_{bright}(k)$, and camera identifiers k and l. If camera l has a filled-in BRF, is totally obscured, or is lacking valid angular data, it is not used to test the fit of the deterministic model using the above equation. If no l exists that can be used, deterministic modeling is automatically assumed to be successful. The index i_{azim} depends on l (as opposed to k) because the expected accuracy of δA_k (based on the BRF measurement by camera l) depends on the relative azimuth of camera l, and not k. Typically the values of Δ_d are around 0.01. If the condition in Eq. (9) is not met for Ice or Liquid clouds, Stochastic modeling must be checked for this camera angle.

For scenes with Unknown cloud phase that do not meet the Δ_d threshold test, check to see whether use of the Liquid model (i.e., the model identified by the same set of indices except with i_{phase} changed from the Unknown to the Liquid designation) enables the test to be passed. If it passes, continue with Deterministic modeling but flag this angle as having required substitution of the Liquid model. If the test fails, Stochastic modeling must be checked for this camera angle.

If a deterministic model has been successfully found, compute

$$\delta A_k = u_k(\delta A_{kk} + \delta A_{k, k-1} + \delta A_{k, k+1})/3 \qquad \text{for any camera other than Df or Da}$$

$$\delta A_k = u_k(\delta A_{kk} + \delta A_{k, k+1})/2 \qquad \text{for camera Df}$$

$$\delta A_k = u_k(\delta A_{kk} + \delta A_{k, k-1})/2 \qquad \text{for camera Da} \tag{10}$$

No cameras (l) that have a filled-in BRF, are totally obscured, or do not contain valid angular data are to be used to calculate the value of δA_k.

3.4.2.1.2 Stochastic method

If $\mu_0 \leq 0.9$ and $k \neq 5$, and a suitable plane-parallel model could not be identified by following the Deterministic methodology of §3.4.2.1.1, we check the suitability of Stochastic modeling to obtain the coefficients needed to evaluate Eq. (7). Stochastic modeling is automatically assumed to be successful for all camera angles (k) which are not totally obscured and have a filled-in BRF.

For all camera angles where Deterministic modeling failed, we use the already-established index numbers to find the values of w_{kl} and ε_k for the appropriate stochastic model in the AZM Dataset that corresponds to the proper conditions [i_{sun}, $i_{view\_zenith\_angle}(l)$, $i_{azim}(l)$, $i_{igloo}(k)$, i_{band}, i_{surf}, i_{phase}, i_{alt}], noting that i_{azim}, and i_{igloo} depend on camera angle and i_{alt} depends on spectral band. [Note that the index numbers related to the view angle ($i_{view\_zenith\_angle}$ and i_{azim}) are for camera l, not k. This is because δA_k is estimated from the measurement of camera l, whose viewing angle index numbers are often different from those of camera k.] Next, find the values of w_{kl} and ε_k for the neighboring stochastic models for both cloud phases (liquid and ice), and $i'_{azim} = i_{azim} + 1$. Then we determine the actual w_{kl} and ε_k values through a two-dimensional linear interpolation over the relative azimuth and cloud phase (using the actual azimuth value and the probability of liquid cloud phase), while treating all other index numbers as constant. Then, we calculate estimates of δA_{kl} given by

$$\delta A_{kl} = w_{kl}\overline{B}_l + \varepsilon_k \tag{11}$$

for

(1) $l = k$, $l = k + 1$, and $l = k - 1$ for any camera other than Df or Da;

(2) $l = k$ and $l = k + 1$ for camera Df;

(3) $l = k$ and $l = k - 1$ for camera Da.

If δA_{kk} and the other value(s) of δA_{kl} agree, that is, if

$$\left| \delta A_{kl} - \delta A_{kk} \right| \leq \Delta_s \tag{12}$$

for all relevant values of l then stochastic weighting can be used. The values of Δ_s are stored in the AZM Dataset and indexed by i_{sun}, $i_{azim}(l)$, $i_{igloo}(k)$, $i_{bright}(k)$, and camera identifiers k and l. As with Deterministic modeling, if camera l has a filled-in BRF, is totally obscured, or does not contain valid angular data it is not used to test the fit of the stochastic model. If no l exists that can be used, Stochastic modeling is automatically assumed to be successful. The index i_{azim} depends on l (as opposed to k) because the expected accuracy of δA_k (based on the BRF measurement by camera l) depends on the relative azimuth of camera l, and not k. Typically the values of Δ_s are around 0.03. If this condition is not met, Solid Angle Weighting must be used at this camera angle.

Once we have determined which of the nine δA_k values meet the criteria for Deterministic or Stochastic weighting, we can now complete the calculations for the Stochastic case by applying Eq. (11) to all l values. For each l, ($l = 1, 2,..., 9$), we set $g_{kl} = 1$ if l is an angle at which either the Deterministic or Stochastic method has been deemed successful or if $l = 5$; otherwise we set $g_{kl} = 0$. Additionally, if camera l has filled-in BRF data, is totally obscured, or does not contain valid angular data then we set $g_{kl} = 0$. If stochastic modeling is being applied and there are no $g_{kl} = 1$ for any cameras k, we recalculate all values of g_{kl}, this time setting $g_{kl} = 1$ for any cameras that are not totally obscured and do not have filled-in data, regardless of the method used to calculate their δA_k value. Then, for each camera angle k at which Stochastic weighting is to be used, we combine the values of δA_{kl} in a weighted average depending on their expected error, as

$$\delta A_k = \frac{\left(u_k \sum_{l=1}^{9} \frac{g_{kl} \delta A_{kl}}{\sigma_{kl}} \right)}{\left(\sum_{l=1}^{9} \frac{g_{kl}}{\sigma_{kl}} \right)} \tag{13}$$

where σ_{kl} is the RMS error expected in estimating δA_k based on the BRF of camera l. The values of σ_{kl} are precalculated and obtained from the AZM Dataset (see §4.4.4), stored as a function of

the indices i_{sun}, $i_{view\_zenith\_angle}(l)$, $i_{azim}(l)$, $i_{igloo}(k)$, i_{band}, i_{surf}, i_{phase}, i_{alt}, and camera identifiers k and l.

3.4.2.2 Subregions classified as AZM Clear

There are two techniques for determining each contribution, δA_k, to the local albedo for clear skies. In the Deterministic method, a semi-empirical 3-parameter model is first fitted to the average values of $\overline{B}_k$, taking into account the height of the RLRA and the solar and viewing geometry. If 6 or more of the 9 values of $\overline{B}_k$ (excluding values which were filled in by interpolation or extrapolation) closely match this model, then the model is used to determine the δA_k for each of the matching directions (accounting for possible obscuration through the values of u_k). For the non-matching directions, δA_k is calculated using the Solid Angle Weighting method. Otherwise, if fewer than 6 of the clear scene measurements of $\overline{B}_k$ closely match the model, or if more than 3 $\overline{B}_k$ values were filled in by the methodology of §3.3.2, it is not used and Solid Angle Weighting is applied to the entire set of clear scene δA_k values. Solid Angle Weighting is also used at all angles if the solar zenith angle cosine, μ_0, exceeds 0.9.

3.4.2.2.1 Deterministic method

There are several semi-empirical BRF models reported in the literature [9] but only some of them obey directional reciprocity, i.e., the sun and view directions can be interchanged without changing the value of the function. Because violations of reciprocity are specific to the 3-dimensional geometric structure of the surface, and we want to use a model capable of representing general directional reflectance characteristics, we require a model that satisfies reciprocity. The semi-empirical BRF model we use is the Coupled Surface-Atmosphere Reflectance (CSAR) equation of Rahman et al. [22], modified to allow a nearly linearizable least squares fitting analysis. This modified model [8] has been shown to work sufficiently well for representing the bidirectional reflectance of a wide variety of surface types (including water, vegetation, soil, and snow) overlain by different atmospheric models [3], and is also used to facilitate atmospheric corrections over clear skies in the MISR surface retrieval algorithm [M-10]. It is described by

$$B_{model}(-\mu, \mu_0, \phi - \phi_0) = r_0 \cdot [\mu\mu_0(\mu + \mu_0)]^{\kappa - 1} \cdot \exp[\beta \cdot p(\Omega)] \cdot h(-\mu, \mu_0, \phi - \phi_0) \qquad (14)$$

with free parameters (r_0, κ, β). The function h is a factor to account for the backscatter "hot spot",

$$h(-\mu, \mu_0, \phi - \phi_0) = 1 + \frac{1 - r_0}{1 + G(-\mu, \mu_0, \phi - \phi_0)} \qquad (15)$$

with

$$G(-\mu, \mu_0, \phi - \phi_0) = \left\{ \left(\frac{1}{\mu^2} - 1 \right) + \left(\frac{1}{\mu_0^2} - 1 \right) + 2 \left[\sqrt{\left(\frac{1}{\mu^2} - 1 \right)\left(\frac{1}{\mu_0^2} - 1 \right)} \right] \cos(\phi - \phi_0) \right\}^{\frac{1}{2}} \qquad (16)$$

The function p in Eq. (14) is assumed to depend only on the scattering angle Ω, the angle between the directions of the incident and reflected radiances, and at the present time it is defined to be

$$p(\Omega) = \cos\Omega \qquad (17)$$

where $\cos\Omega$ is calculated according to Eq. (6).

Rather than fit Eq. (14) directly to the MISR clear-sky BRF's, we have found from algorithm testing that accuracy improvements can be gained in many instances if we first implement a Rayleigh pre-correction to the observed BRF's. The corrected value is of the form:

$$\overline{B_{k, corr}} = (\overline{B_k} - B_{Rayleigh}) \exp\left(\frac{\tau_R}{\mu} \right) \qquad (18)$$

where $B_{Rayleigh}$ is the BRF due to Rayleigh scattering, and τ_R is the Rayleigh scattering optical depth. Since the Rayleigh pre-correction need not be exact, the following methodology is used. Rayleigh optical depth at the standard surface pressure of 1013.25 hPa is specified to have the standard values, $\tau_{R,s}$, of 0.240, 0.094, 0.043, and 0.015 for MISR bands 1 - 4, respectively. Scaling to the ambient pressure is accomplished as follows:

$$\tau_R = \tau_{R, s} \cdot \exp\left(-\frac{RLRA}{H} \right) \qquad (19)$$

where H is the atmospheric scale height, which we set to 8 km. The Rayleigh BRF term is computed using the method developed by Vermote and Tanre [31], which uses sun and view geometry and τ_R as input and returns $B_{Rayleigh}$ as output.

The correction described by Eq. (18) is only applied in the event that the subregion is classified as High Cloud Not Present in §3.4.1. If the subregion was classified as High Cloud Present or High Cloud Undetermined, the Rayleigh pre-correction is not applied, that is, we set $\tau_R = 0$, $B_{Rayleigh} = 0$, and $\overline{B_{k, corr}} = \overline{B_k}$. This is because the ASCM detects high cloud using a detection method that relies upon the cloud being situated above the bulk of the Rayleigh-scattering atmosphere. Thus, in this case the Rayleigh optical depth above the reflecting layer is close to zero. Simulations have shown that the BRF model of Eq. (14) is typically capable of reproducing angular reflectances even when the Rayleigh scattering is not removed; however, we include the correction where feasible to improve accuracy at oblique solar zenith angles.

Determination of the values of δA_k is now performed. If there are 3 or fewer camera angles that required filling in missing data according to §3.3.2, we perform a least-squares fit of $\overline{B_{k,\,corr}}$ (excluding those corresponding to filled-in data) to B_{model} in order to determine the parameters (r_0, κ, β). If more than 3 angles required filling in of missing data, we default to the Solid Angle Weighting method for all values of δA_k.

The fitting of $\overline{B_{k,\,corr}}$ to B_{model} is accomplished iteratively by taking the logarithm of each value and minimizing the sum of the squares of the residuals,

$$S = \sum_k [\ln \overline{B_{k,\,corr}}(-\tilde{\mu}_k, \mu_0, \phi_k - \phi_0) - \ln B_{model}^{(n)}(-\tilde{\mu}_k, \mu_0, \phi_k - \phi_0)]^2 \tag{20}$$

where the summation is over the camera angles used and

$$\ln B_{model}^{(n)}(-\tilde{\mu}_k, \mu_0, \phi_k - \phi_0) = \ln r_0^{(n)} + (\kappa^{(n)} - 1) \cdot \ln[\tilde{\mu}_k \mu_0 (\tilde{\mu}_k + \mu_0)] +$$
$$+ \beta^{(n)} \cdot p(\Omega_k) + \ln h^{(n)}(-\tilde{\mu}_k, \mu_0, \phi_k - \phi_0) \tag{21}$$

Note that in Eqs. (20) and (21) we use the notation $\tilde{\mu}_k$ to denote the actual view zenith angle of the kth camera as determined by the Level 1B2 geometric parameters, not the nominal angles used in the AZM Dataset.

The model is given explicit dependence on the iteration count through the superscript (n) because the parameters are updated every time an iteration is performed. Aside from the $\ln h^{(n)}$ term in Eq. (21), we note that $\ln B_{model}$ is linear in the three model parameters $\ln r_0$, κ, and β. The $\ln h^{(n)}$ term, which contains r_0, is easily handled by simply using the value of r_0 from the previous iteration. Thus, from Eq. (15),

$$h^{(n)}(-\mu, \mu_0, \phi - \phi_0) = 1 + \frac{1 - r_0^{(n-1)}}{1 + G(-\mu, \mu_0, \phi - \phi_0)} \tag{22}$$

where $r_0^{(-1)}$ is set equal to zero.

The minimization of S in Eq. (20) follows conventional least-squares methodology, in which we establish three equations, $\partial S / \partial \ln r_0^{(n)} = 0$, $\partial S / \partial (\kappa^{(n)} - 1) = 0$, and $\partial S / \partial \beta^{(n)} = 0$ to solve for $r_0^{(n)}$, $\kappa^{(n)}$, and $\beta^{(n)}$. Letting K be the number of camera angles included in the summation of Eq. (20), and

$$\Upsilon_k^{(n)} = \ln \overline{B_{k,\,corr}}(-\tilde{\mu}_k, \mu_0, \phi_k - \phi_0) - \ln h^{(n)}(-\tilde{\mu}_k, \mu_0, \phi_k - \phi_0) \quad , \tag{23}$$

$$m_k = \ln[\tilde{\mu}_k \mu_0 (\tilde{\mu}_k + \mu_0)] \quad , \tag{24}$$

then

$$\begin{bmatrix} \ln r_0^{(n)} \\ \kappa^{(n)} - 1 \\ \beta^{(n)} \end{bmatrix} = \begin{bmatrix} K & \sum_k m_k & \sum_k p(\Omega_k) \\ \sum_k m_k & \sum_k (m_k)^2 & \sum_k m_k p(\Omega_k) \\ \sum_k p(\Omega_k) & \sum_k m_k p(\Omega_k) & \sum_k p^2(\Omega_k) \end{bmatrix}^{-1} \begin{bmatrix} \sum_k \Upsilon_k^{(n)} \\ \sum_k m_k \Upsilon_k^{(n)} \\ \sum_k p(\Omega_k) \Upsilon_k^{(n)} \end{bmatrix} \tag{25}$$

from which it is straightforward to obtain $r_0^{(n)}$, $\kappa^{(n)}$, and $\beta^{(n)}$. The value of $r_0^{(n)}$ is used to update Eqs. (22) and (23), and new values of the parameters are obtained from Eq. (25). This process repeats, and generally only a few iterations are required. Rather than stipulate a convergence test, we let this process run for a fixed number of iterations, n_{iter}. We set $n_{iter} = 4$.

We now test whether an adequate fit has been obtained. At each camera angle that was used in the fit we compute:

$$\chi_k^2 = \frac{\mu_0^2 (\overline{B_{k,\,corr}} - B_{model})^2}{\sigma_{cam,\,k}^2} \tag{26}$$

where $\sigma_{cam,k}$ is the relative camera-to-camera radiometric uncertainty in equivalent reflectance, where equivalent reflectance is equal to $\mu_0 \overline{B_{k,\,corr}}$. The value of $\sigma_{cam,k}$ is obtained by using calibration uncertainty information provided in the MISR Ancillary Radiometric Product (see *[M-5]*). These data are provided at a standard set of equivalent reflectances (nominally 15 values), for each channel (band and camera combination) of the instrument. Specifically, we make use of:

(1) ε_{cam_sys}, the systematic component of the camera-to-camera relative radiometric uncertainty, expressed in percent, at the tabulated set of equivalent reflectance levels and in the appropriate channel;

(2) SNR_{am}, the signal-to-noise ratio at the tabulated set of equivalent reflectance levels and in the appropriate channel, for the averaging mode *am* = 4x4. (We are actually computing BRF's on 2.2-km centers, which would correspond to 8x8 averaging, but given the presence of systematic error a correction is not warranted.)

Now, to calculate $\sigma_{cam,\,k}$ corresponding to equivalent reflectance $\rho_k = \mu_0 \overline{B_{k,\,corr}}$, we first linearly interpolate the tabulated values of ε_{cam_sys} and SNR_{4x4} to this equivalent reflectance. Denoting these interpolated values $\varepsilon_{cam\_sys}(\rho_k)$ and $SNR_{4x4}(\rho_k)$, we then have

$$\sigma_{cam,\,k}^2 = \rho_{MISR,\,k}^2 \left\{ \left(\frac{\varepsilon_{cam\_sys}(\rho_k)}{100} \right)^2 + \left(\frac{1}{SNR_{4x4}(\rho_k)} \right)^2 \right\} \tag{1a}$$

Next, we check to see that there are at least 6 camera angles for which $\chi_k^2 < 2$. Referring to Eq. (26), this means that the model fit deviates from the observations by no more than twice the instrument uncertainty. If less than 6 camera angles satisfy this criterion, default to Solid Angle Weighting for the entire set of angles.

If an adequate fit has been obtained in a given spectral band, a camera-averaged goodness-of-fit parameter is calculated and archived with the data product. This parameter is given by

$$\chi_{avg}^2 = \frac{1}{N_{cam}} \sum_k \chi_k^2 \tag{2b}$$

where the summation is over the N_{cam} camera angles used in the BRF model fitting. The BRF model is then used to calculate δA_k for those angles for which $\chi_k^2 < 2$. For the remaining angles, δA_k is determined using Solid Angle Weighting. For those angles at which the model fit is used to calculate δA_k, the algorithm is:

$$\delta A_k = \frac{u_k \overline{B_{k,\,corr}}(-\tilde{\mu}_k, \mu_0, \phi_k - \phi_0)}{\pi B_{model}(-\tilde{\mu}_k, \mu_0, \phi_k - \phi_0)} \int_{\mu_{k,\,lower}}^{\mu_{k,\,upper}} \int_{\phi_{k,\,lower}}^{\phi_{k,\,upper}} B_{model}(-\mu, \mu_0, \phi - \phi_0) \exp\left(-\frac{\tau_R}{\mu}\right) \mu\, d\mu\, d\phi$$

$$+ \frac{u_k}{\pi} \int_{\mu_{k,\,lower}}^{\mu_{k,\,upper}} \int_{\phi_{k,\,lower}}^{\phi_{k,\,upper}} B_{Rayleigh}(-\mu, \mu_0, \phi - \phi_0) \mu\, d\mu\, d\phi \tag{27}$$

where the integration limits are the solid angle bin boundaries defined in §3.3.1 for azimuth ϕ and §4.4.1 for cosine of the view zenith angle μ (based on nominal view geometry). The scaling term $\overline{B_{k,\,corr}}/B_{model}$ included in front of the integral in the first term on the right hand side of Eq. (27) has a value ≈ 1, and is included to insure that the model fit primarily influences the azimuthal correction, while the data maintain the absolute scaling.

The integrals in Eq. (27) are evaluated by subdividing the solid angle bins into arrays of N_μ

x N_ϕ sub-bins. We set $N_\mu = 10$ and $N_\phi = 90$. For each bin over which the integration is performed, we let

$$\Delta\mu = \frac{|\mu_{k,\,upper} - \mu_{k,\,lower}|}{N_\mu} \tag{28}$$

$$\Delta\phi = \frac{\pi}{N_\phi} \tag{29}$$

Then, if we let

$$\mu_i = \mu_{k,\,lower} + \left(i - \frac{1}{2}\right)\Delta\mu \tag{30}$$

$$\phi_j = \phi_{k,\,lower} + \left(j - \frac{1}{2}\right)\Delta\phi \tag{31}$$

then letting $F(-\mu, \mu_0, \phi - \phi_0)$ represent the integrand of either of the above integrals,

$$\int_{\mu_{k,\,lower}}^{\mu_{k,\,upper}} \int_{\phi_{k,\,lower}}^{\phi_{k,\,upper}} F(-\mu, \mu_0, \phi - \phi_0)\mu\, d\mu\, d\phi \cong \Delta\mu\Delta\phi \sum_{i=1}^{N_\mu} \sum_{j=1}^{N_\phi} F(-\mu_i, \mu_0, \phi_j - \phi_0)\mu_i \tag{32}$$

3.4.2.3 Solid Angle Weighting method

If any of the following conditions occur:

(1) $\mu_0 > 0.9$;

(2) $k = 5$ (i.e., we are dealing with the nadir camera) and the subregion is classified as AZM Cloud;

(3) Neither Deterministic (cloud), Stochastic (cloud), nor Deterministic (clear) methodologies meet the required criteria;

(4) The $(2.2\text{-km})^2$ subregion is classified as AZM Undetermined;

(5) The $i_{igloo}(k)$ index number could not be calculated due to missing angular data in both the Df and Da cameras;

then the Solid Angle Weighting method is used to determine δA_k. This is mainly a matter of numerical integration, allowing for the possibility of discrete changes in obscuration from one

camera to the next, whereby the 9 discrete measurements of BRF are summed using weights that involve no model assumptions about the azimuthal dependence of BRF.

The albedo contributions for solid angle weighting are written:

$$\delta A_1 \;=\; u_1 w_{11} \overline{b_1} + u_2 w_{12} \overline{b_2}$$

$$\delta A_k \;=\; \sum_{l=k-1}^{k+1} u_l w_{kl} \overline{b_l} \qquad 2 \le k \le 8; \qquad k \ne 5$$

$$\delta A_5 \;=\; u_4 w_{54} \overline{b_4} + w_{55} \overline{b_5} + u_6 w_{56} \overline{b_6}$$

$$\delta A_9 \;=\; u_8 w_{98} \overline{b_8} + u_9 w_{99} \overline{b_9} \tag{33}$$

where generally $\overline{b_l} = \overline{B_l}$. However, if the index l corresponds to one of the k indices for which a value of δA_k has already been calculated using either the Deterministic (cloud), Stochastic (cloud), or Deterministic (clear) method, and $u_l \ne 0$, we take advantage of the azimuthal correction already found for this index by instead setting

$$\overline{b_l} \;=\; \frac{\delta A_l}{u_l c_l} \tag{34}$$

where the c_l values are precalculated in the AZM Dataset and discussed in §4.4.4.2.1. Note that a value of c_5 is not needed because neither the Deterministic (cloud), Stochastic (cloud), nor Deterministic (clear) methods are ever used for the nadir camera.

There are several special cases called out in Eq. (33):

(1) δA_1 and δA_9 because these solid angle bins are neighbored by only one camera.

(2) δA_5 because the coefficient in front of $\overline{b_5}$ takes a special form.

For situations in which the relevant values of $u_k \overline{b_k}$ are nonzero, the precalculated weights w_{kl} are obtained from the AZM Dataset (see §4.4.4.2.2). Exceptions to this are w_{11}, w_{55}, and w_{99}, The weights w_{11}, w_{55}, and w_{99} must be determined during the retrieval processing because they depend on the unobscured fractions u_1, u_5, and u_9, which precludes precalculation. The required equations are:

$$w_{11} = \frac{\mu_1}{8}(3\mu_2 + \mu_1) - \frac{\mu_1^2(1 - u_1)}{2\sqrt{1 - \mu_1^2 + \mu_1^2(1 - u_1)^2}} \tag{35}$$

$$w_{55} = \frac{\mu_5}{8}\left[\frac{8}{\mu_5} - 8 + u_5(8 - 2\mu_5 - 3\mu_4 - 3\mu_6)\right] \tag{36}$$

$$w_{99} = \frac{\mu_9}{8}(3\mu_8 + \mu_9) - \frac{\mu_9^2(1 - u_9)}{2\sqrt{1 - \mu_9^2 + \mu_9^2(1 - u_9)^2}} \tag{37}$$

where the μ-values are the nominal ones, as listed in Table 5. In the derivation of Eq. (36), we have made the assumption that $\bar{b}$ is constant for $\mu_5 \leq \mu \leq 1$. Note that in the event that $u_5 = 0$, the value of w_{55} is set to 0. In the derivation of Eqs. (35) and (37) (for $k = 1$ or $k = 9$), we have assumed that $\bar{b}_k$ is constant for $0 \leq \mu \leq \mu_k$, and that the unobscured fraction depends continuously on view angle θ across the bin according to

$$u = 1 - f_k\tan\theta = 1 - f_k\frac{\sqrt{1 - \mu^2}}{\mu} \qquad \text{for } \mu_{min} \leq \mu \leq \mu_k \tag{38}$$

$$= 0 \qquad \text{for } 0 \leq \mu \leq \mu_{min}$$

where u is considered to be a continuous, not discrete, variable in Eq. (38) and where

$$f_k = \frac{1 - u_k}{\tan\theta_k} = \frac{(1 - u_k)\mu_k}{\sqrt{1 - \mu_k^2}} \tag{39}$$

and

$$\mu_{min} = \frac{(1 - u_k)\mu_k}{\sqrt{1 - \mu_k^2 + \mu_k^2(1 - u_k)^2}} \tag{40}$$

which is the value of μ at which the unobscured fraction equals zero.

3.4.3   Calculate local albedo

The local albedo is now calculated from the individual δA_k values by applying Eq. (1).

43

3.5 THEORETICAL DESCRIPTION: RESTRICTIVE ALBEDO

3.5.1 Calculate restrictive albedo

The restrictive albedo is determined by summing the unobscured fluxes associated with all the local 2.2 km albedos across the $(35.2\text{-km})^2$ region, together with the side-leaving BRF's that have not been used in determining the local albedos because they are associated with side views brought about by changes in the altitude of local RLRA's. We explicitly include the solar zenith angle cosine, μ_0, in the calculations because the underlying physics requires the averaging of fluxes, not albedos, and we must allow for the possibility of variation in μ_0 over the $(35.2\text{-km})^2$ region.We take such variations into account by obtaining μ_0 from Level 1B2 on 17.6-km centers, and assuming μ_0 is constant for each $(17.6\text{-km})^2$ region. However, if any of the four values of μ_0 within the $(35.2\text{-km})^2$ region is < 0.04, the restrictive albedo is not calculated. The restrictive albedo is also not calculated if the solar zenith angle is missing.

The flux contribution of the side-leaving BRF's does not involve an azimuthal correction, and the required weights, q_{kk}, are based upon solid angle weighting, and obtained from the AZM Dataset (see §4.4.4.2.3). A renormalization of the side-leaving term is included to compensate for the possibility of missing data at one or more view angles.

The restrictive albedo is expressed as the sum of a top-leaving term and a side-leaving term:

$$A_{\text{restrictive}} = A^{top}_{\text{restrictive}} + A^{side}_{\text{restrictive}} \tag{41}$$

and is calculated for each spectral band separately.

3.5.1.1 Top-leaving contribution to restrictive albedo

The top-leaving term is the simpler of the two and is given by

$$A^{top}_{\text{restrictive}} = \frac{\sum_x \sum_y e(x, y) \cdot \mu_0(x, y) \cdot A_{\text{local}}(x, y)}{\langle \mu_0 \rangle N} \tag{42}$$

where

> $e(x, y) = 1$ if a value of A_{local} is available at location (x, y); else $e(x, y) = 0$ if A_{local}
> does not exist due to (a) missing $\overline{B_k}$ for all k with $u_k > 0$, (b) $\mu_0 < 0.04$, or (c) no
> retrieved value of RLRA;

$\langle \mu_0 \rangle$ is an effective solar zenith angle cosine, given by the average of the four values of μ_0 provided on 17.6-km centers (by Level 1B2) within the $(35.2\text{-km})^2$ region. Missing values of the solar zenith angle are not included in this average;

N is the number of subregions at which $e(x, y) = 1$, given by

$$N = \sum_x \sum_y e(x, y) \, , \tag{43}$$

where typically $1 \le N \le 256$, since there are 256 $(2.2\text{-km})^2$ subregions in the $(35.2\text{-km})^2$ region. We note that if there are no available values of A_{local}, then $N = 0$, and we skip the remaining steps and neither $A_{\text{restrictive}}^{top}$ nor $A_{\text{restrictive}}$ is calculated.

3.5.1.2   Side-leaving contribution to restrictive albedo

The side leaving term is given by

$$A_{\text{restrictive}}^{side} = \frac{\sum_{k=1}^{9} \delta_k q_{kk} S_k}{\sum_{k=1}^{9} \delta_k q_{kk}} \tag{44}$$

where we define S_k to be

$$S_k = \frac{1}{\langle \mu_0 \rangle M_k} \sum_x \sum_y f_k(x, y) \cdot \mu_0(x, y) \cdot v_k(x, y) \cdot \overline{B_{\text{sides}, k}}(x, y) \qquad \text{for } M_k \ne 0$$

$$= 0 \qquad \text{for } M_k = 0 \tag{45}$$

and

$f_k(x, y)$ indicates whether or not a value of $\overline{B_{\text{sides}, k}}$ exists at location *(x, y)* [i.e., radiometric data are available, either from earlier TOA/cloud processing *[M-8]* or by extrapolation/interpolation (§3.3.3)]. Note that we make an important distinction between $\overline{B_{\text{sides}, k}}$ being unavailable due to absence of radiometric data at camera angle *k* (e.g., due to the failure of an instrument channel and no nearby angles being available either), as opposed to the case where $v_k(x, y) = 0$, that is, where the column side is completely obscured. Thus, if a value of $\overline{B_{\text{sides}, k}}(x, y)$ exists or if $v_k(x, y) = 0$, we set $f_k(x, y) = 1$; but if $v_k(x, y) \neq 0$ and a value of $\overline{B_{\text{sides}, k}}(x, y)$ does not exist, $f_k(x, y) = 0$;

$\overline{B_{\text{sides}, k}}$ is the average side-leaving BRF for camera *k* associated with each of the $(2.2\text{-km})^2$ columns within the $(35.2\text{-km})^2$ region;

v_k is the unobscured pixel ratio, $s_k / 64$, of the side of the RLRA, given s_k unobscured 275-m pixels for the kth camera on the side of the RLRA column. Unlike u_k, the unobscured fraction of the RLRA top, for which $0 \leq u_k \leq 1$, it is possible for v_k to be larger than unity. This arises because the area over which the side leaving energy emanates is given by $(275 \text{ m})^2 s_k$, and the height of the RLRA column can be such that $s_k > 64$. Since the summation in Eq. (45) is over subregions of area $(2.2 \text{ km})^2$, we replace the term $(275 \text{ m})^2 s_k$ by $(2.2 \text{ km})^2 (s_k / 64)$, which is equal to $(2.2 \text{ km})^2 v_k$, in deriving Eq. (45);

M_k is the number of locations [typically $1 \leq M_k \leq 256$, since there are 256 $(2.2\text{-km})^2$ subregions in the $(35.2\text{-km})^2$ region] at which $f_k(x, y) = 1$, given by

$$M_k = \sum_x \sum_y f_k(x, y) ; \qquad (46)$$

q_{kk} are solid angle weights for adding the contribution of the side-leaving BRF's, obtained from the AZM Dataset (see §4.4.4.2.3);

and $\delta_k = 1$ if $M_k > 0$ and $\delta_k = 0$ if $M_k = 0$ [i.e., if are no available values of $\overline{B_{\text{sides}, k}}$ at any *(x, y)*].

Eq. (44) compensates for missing values of S_k by normalizing to the solid angle over which valid

data exist.

Technically, the division by $\langle\mu_0\rangle$ in Eqs. (42) and (44) is not exactly rigorous, because it represents the average μ_0 value over all locations within the $(35.2\text{-km})^2$ region, rather than only where valid values of A_{local} or $\overline{B}_{\text{sides, }k}$ exist. However, because μ_0 varies slowly over the region, and in the nominal case data will be available at all 256 $(2.2\text{-km})^2$ subregions within the region, the chances of introducing error due to this approximation are extremely small, and thus we do not believe any additional complexity in the formulation is warranted.

We note that if values of S_k could not be calculated at the entire set of 9 angles, that is, $M_k = 0$ for every value of k, neither $A_{\text{restrictive}}^{side}$ nor $A_{\text{restrictive}}$ is calculated.

3.6 THEORETICAL DESCRIPTION: EXPANSIVE ALBEDO

3.6.1 Calculate expansive albedo

The expansive albedo is found as a horizontal integration of the relevant BRF's from the RLRA top surfaces, together with the side-leaving BRF's. It is calculated for each spectral band separately.

For computational efficiency we currently evaluate the expansive albedo at the center of each $(35.2\text{-km})^2$ grid only, expecting the values across this grid area to be highly correlated because of the smoothing effect of the large area integration implicit in the definition. Calculating the area average over the $(35.2\text{-km})^2$ grid area can be done by direct repetition; however, this is presently not anticipated to be worth the additional computer time. As with the restrictive albedo, if any of the four values of μ_0 within the $(35.2\text{-km})^2$ region is < 0.04, the expansive albedo is not calculated. Additionally, points lying outside the $(35.2\text{-km})^2$ region are excluded from contributing to the expansive albedo if they are at locations where $\mu_0 < 0.04$. The expansive albedo cannot be calculated if $\langle\mu_0\rangle$ does not exist due to missing solar zenith angle data.

We note that the integral over solid angle to get upwelling irradiance through a surface at altitude z above a plane surface can be rewritten as an area integral, in terms of (x, y, z), as

$$\int_0^{2\pi}\int_0^1 L\mu\, d\mu\, d\phi = \int_{-\infty}^{\infty}\int_{-\infty}^{\infty} L\frac{(\cos\theta)^2}{R^2}dxdy = \int_{-\infty}^{\infty}\int_{-\infty}^{\infty} L\frac{z^2}{(x^2+y^2+z^2)^2}dxdy \ , \tag{47}$$

where the $+x$ axis points in the flight (along-track) direction, $+z$ points downward (toward the Earth), and $+y$ is the cross product of the $+z$ and $+x$ axes, and points cross-track; L is radiance; and R is the distance between the centers of the upper and lower regions. Note that Eq. (47) does not presently include the effect of Earth curvature. Later algorithm revisions will include this if

47

necessary.

Including possible changes in solar zenith angle over the area of integration, the expansive albedo is calculated as the sum:

$$A_{expansive} = \frac{(2.2)^2 F}{\pi \langle \mu_0 \rangle} \cdot$$

$$\cdot \sum_x \sum_y \mu_0(x, y) \frac{z^2(x, y)}{[x^2 + y^2 + z^2(x, y)]^2} [\overline{b}_k(x, y) + v_k(x, y) \overline{B}_{sides, k}(x, y)]$$

(48)

where k is the nearest camera angle that matches the vector between (x, y) on the RLRA and the 30-km altitude grid center (determined as described below), and F is a solid angle normalization factor to take into account that we may not have data at all (x, y) in the integration area. This will occur especially as the swath edge is approached, so by including F the expansive albedo is correctly normalized over the available solid angle. What this means in practice is that the expansive albedos will maintain consistent values from the center to the edge of the swath, but by the time the edge values are calculated they will be based on about half the data that the center values are based upon, and will consequently be more variable. F is given by:

$$F = \pi \left[(2.2)^2 \sum_x \sum_y \frac{z^2(x, y)}{[x^2 + y^2 + z^2(x, y)]^2} \right]^{-1}$$

(49)

so we get the final result:

$$A_{expansive} = \frac{\sum_x \sum_y \mu_0(x, y) \frac{z^2(x, y)}{[x^2 + y^2 + z^2(x, y)]^2} [\overline{b}_k(x, y) + v_k(x, y) \overline{B}_{sides, k}(x, y)]}{\langle \mu_0 \rangle \sum_x \sum_y \frac{z^2(x, y)}{[x^2 + y^2 + z^2(x, y)]^2}}$$

(50)

where

the x, y summation is over the $(2.2\text{-km})^2$ grid centers, located x km and y km from the center of the $(35.2\text{-km})^2$ region in the x and y directions;

the value of z is given by

48

$$z(x, y) = 30 \text{ km} - RLRA(x, y) ; \tag{51}$$

$\langle \mu_0 \rangle$ is the average of the four values of μ_0 available from Level 1B2 within the $(35.2\text{-km})^2$ region associated with the expansive albedo, identical to $\langle \mu_0 \rangle$ in §3.5.1;

and $\overline{b}_k(x, y)$ is an effective BRF calculated algorithmically as follows:

(1) Find the nearest k that matches the vector between (x, y) on the RLRA and the 30-km altitude grid center. This is done using the following method. If $x \geq 0$, then the nearest k is selected from the set $\{1, 2, ..., 5\}$, and if $x < 0$, the nearest k is selected from the set $\{5, 6, ..., 9\}$. Then we compute

$$\mu = \frac{z(x, y)}{\sqrt{x^2 + y^2 + z^2(x, y)}} \tag{52}$$

and find the value of k for which $|\mu - \mu_k|$ is minimized. If any of the viewing zenith angles are missing for the subset of camera angles being searched then the nominal viewing zenith angles are used instead in the above equation.

(2) Use the corresponding value of δA_k already found for that RLRA during the calculation of its local albedo.

(3) Set $\overline{b}_k(x, y) = \dfrac{\delta A_k(x, y)}{q_{kk}}$, where q_{kk} are the same weights used in §3.5.1.2, and are defined in the AZM Dataset.

The summations in Eq. (50) do not include locations (x, y) for which any of the following conditions occur:

(1) $\overline{b}_k(x, y)$ could not be calculated, because $\delta A_k(x, y)$ does not exist. Since interpolation/extrapolation is used for any missing top-leaving BRF's (§3.3.2), a missing value of δA_k can arise when (a) $u_l(x, y) > 0$ for one or more l, and a top-leaving BRF is not available for all of these same l, (b) $\mu_0 < 0.04$, or (c) there was no retrieved value of the RLRA;

(2) $\overline{B}_{\text{sides}, k}(x, y)$ does not exist. This means that $v_k(x, y) > 0$, but no side-leaving BRF is available or filled in at this angle;

(3) $\mu_0(x, y) < 0.04$;

49

(4) The solar zenith angle is missing;

(5) If number of unobscured side pixels is missing;

(6) The absolute value of the along-track distance, $|x|$, exceeds the bounds of the available number of blocks of data, where a block is a portion of the pole-to-pole swath that is 140.8 km in along-track length. We require that all available data from 2 blocks earlier in the swath and 2 blocks later in the swath than the block within which the expansive albedo is being calculated to be included in the summations, for a total of 5 blocks. For expansive albedos calculated on 35.2-km centers, this means that summations over x will be carried out over $|x|$-values ranging from 1.1 km to at least $D_{min} = 298.1$ km (17.6 km + 2 x 140.8 km - 1.1 km), but no more than $D_{max} = 403.7$ km (17.6 km + 3 x 35.2 km + 2 x 140.8 km - 1.1 km), as shown in Figure 9. The summations over y should include all available data in the cross-track swath width of the 5 blocks.
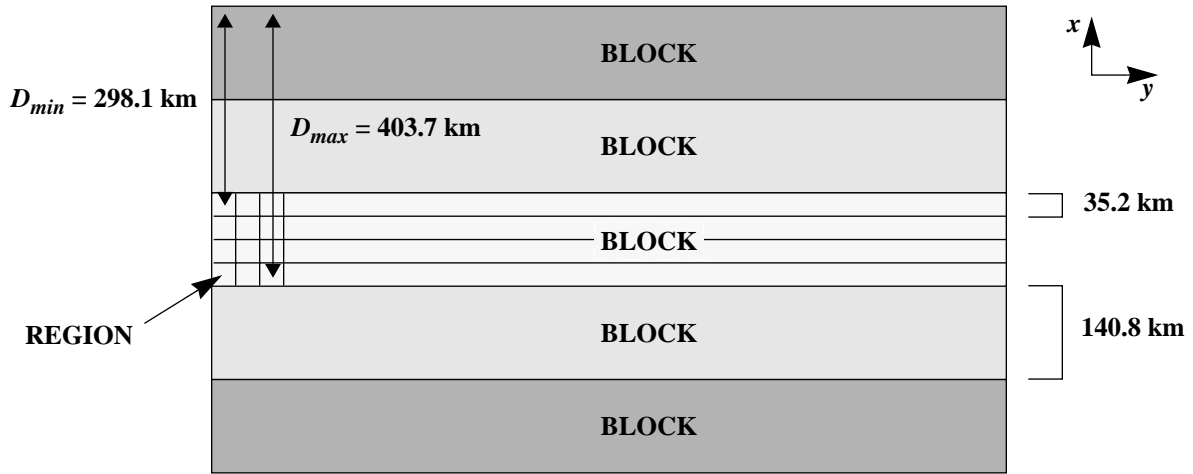
Figure 9. Areas included in calculation of expansive albedo (not to scale)

It may not be immediately obvious that the expansive albedo is being corrected for azimuthal dependences. The local values of δA_k used in Eq. (50) are not adjusted for azimuth direction even though they enter the summation from different azimuthal directions. This works for a complete integration in azimuth provided the δA_k values have already been corrected to have minimal azimuthal bias and we have a large number of individual values so that statistical averaging works in our favor, as is the case here.

3.6.2 Calculate expansive albedo classifiers

The expansive albedo classifiers $F_{\text{ClearHC}}^{\exp}$ and $F_{\text{ClearLC}}^{\exp}$ are designed to establish the fraction of the area over which the summations in Eq. (50) occur that corresponds to Clear with High Confidence, and the fraction which corresponds to Clear with Low Confidence.

The total fractional area contributing to the expansive albedo classified as Clear with High Confidence is:

$$F_{\text{ClearHC}}^{\text{exp}} = \frac{\sum_x \sum_y \sum_{i=1}^{2} \sum_{j=1}^{2} \beta_{i,j}^{ClearHC}[R(i,j), A(i,j), S(i,j)]}{4 \sum_x \sum_y 1} \tag{53}$$

where $R(i, j)$ denotes the feature-projected RCCM with its associated snow/ice indicator, $A(i, j)$ is the ASCM, and $S(i, j)$ is the SDCM, and:

$\beta^{ClearHC} = 1$ if $R(i,j)$ and $A(i,j) = $ ClearHC and the surface is free of snow/ice;

$\beta^{ClearHC} = 1$ if $A(i,j)$ and $S(i,j) = $ Clear and the surface is snow/ice covered;

$\beta^{ClearHC} = 0$ otherwise.

Note that the summations over x and y correspond to the locations of the (2.2-km)^2 subregions that are included in the expansive albedo calculation, Eq. (50). However, since the RCCM, ASCM, and SDCM are defined on (1.1-km)^2 centers, it is necessary to include a summation over the 4 locations contained within the (2.2-km)^2 subregion where the RLRA is defined. This is denoted by the summations over i and j.

The total fractional area contributing to the expansive albedo classified as Clear with Low Confidence is:

$$F_{\text{ClearLC}}^{\text{exp}} = \frac{\sum_x \sum_y \sum_{i=1}^{2} \sum_{j=1}^{2} \beta_{i,j}^{ClearLC}[R(i,j), A(i,j), S(i,j)]}{4 \sum_x \sum_y 1} \tag{54}$$

where

$\beta^{ClearLC} = 1$ if $R(i,j) = $ ClearLC and $A(i,j) = $ ClearLC or ClearHC, or $A(i,j) = $ ClearLC and $R(i,j) = $ ClearLC or ClearHC, and the surface is free of snow/ice;

$\beta^{ClearLC} = 1$ if $S(i,j) = $ NearSurface and $A(i,j) = $ ClearLC or ClearHC, or $A(i,j) = $ ClearLC and $S(i,j) = $ NearSurface or Clear, and the surface is snow/ice covered;

$\beta^{ClearLC} = 0$ otherwise.

51

3.7 PRACTICAL CONSIDERATIONS

3.7.1 Numerical computation considerations

Requirements on processing speed and data storage are described in *[M-16]*.

3.7.2 Programming and procedural considerations

Guidelines to be followed during algorithm development are described in *[M-12]*.

3.7.3 Configuration of retrievals

A TOA Albedo Configuration File is used to establish the numerical values of adjustable parameters used within the retrievals. The purpose of establishing a separate file is to avoid "hard-wiring" specific values into the software. The TOA/Cloud Product will contain information indicating what version of the configuration file was used. The contents of the TOA Albedo Configuration File are shown in Table 4. The values shown correspond to the at-launch settings. The column entitled "Section" indicates where in this ATB a description of the specific configuration parameter is found.

Table 4: Contents of the TOA Albedo Configuration File

Parameter	Value	Section
Minimum value of μ_0 for calculation of albedos	0.04	3.3, 3.6.1
Threshold on camera proximity for filling in missing top-leaving BRF's, Δk_{top}	8	3.3.2
Threshold on camera proximity for filling in missing side-leaving BRF's, Δk_{side}	1	3.3.3
Minimum temperature for setting cloud phase = Liquid	0°C	3.4.2.1.1
Maximum temperature for setting cloud phase = Ice	-43°C	3.4.2.1.1
Minimum number of angles needed for applying Deterministic (clear) model	6	3.4.2.2.1
Standard Rayleigh optical depth, band 1	0.240	3.4.2.2.1
Standard Rayleigh optical depth, band 2	0.094	3.4.2.2.1
Standard Rayleigh optical depth, band 3	0.043	3.4.2.2.1
Standard Rayleigh optical depth, band 4	0.015	3.4.2.2.1
Atmospheric scale height, H	8 km	3.4.2.2.1
Number of iterations for clear sky Deterministic model fit	4	3.4.2.2.1
Threshold for determining goodness of clear-sky AZM fit, χ_k^2	2.0	3.4.2.2.1
Number of cosine of zenith angle sub-bins, N_μ	10	3.4.2.2.1

Table 4: Contents of the TOA Albedo Configuration File (continued)

Parameter	Value	Section
Number of azimuth angle sub-bins, N_ϕ	90	3.4.2.2.1
Minimum value of μ_0 above which pure Solid Angle Weighting is used	0.9	3.4.2.3
TOA altitude for referencing expansive albedos	30 km	3.6.1
Number of 140.8-km blocks contributing to expansive albedo calculation	5	3.6.1

3.7.4 Quality assessment and diagnostics

Several parameters will be reported as part of the TOA/Cloud Product which will serve as diagnostics of how the albedo retrievals are performing. Maps or other summaries of these parameters will be reviewed by the MISR team for quality assessment purposes. These parameters are described in *[M-17]*. References to sections in this ATB containing descriptions of specific retrieval quality indicators are provided in that document.

3.7.5 Exception handling

Missing data are handled as discussed throughout this document.

3.7.6 Algorithm validation

Details on planned field campaigns, experimental methodologies, and instrument calibration and data reduction procedures are documented in *[M-15]*.

4. ALGORITHM DESCRIPTION: SCF PROCESSING

4.1 AZM DATASET CONTENTS

Generation of the albedo parameters of the MISR Level 2 TOA/Cloud Product is preceded by creating, at the MISR SCF, the Azimuthal Model (AZM) Dataset. This occurs prior to launch, and the AZM Dataset is delivered to the DAAC for use during routine processing. The theoretical background behind generation of the parameters of the AZM Dataset is described below. The contents of the AZM Dataset are shown in Table 5.

Table 5: Contents of the AZM Dataset

Parameter	Description	Units
Model index locators		
i_{sun}	Solar zenith angle index number	none
$i_{view\_zenith\_angle}$	View zenith angle index number	none
i_{azim}	View-sun relative azimuth angle index number	none
i_{igloo}	Index number specifying igloo orientation relative to forward/ backward scattering	none
i_{alt}	Altitude (RLRA) bin index number	none
i_{phase}	Cloud phase index (liquid, ice, unknown)	none
i_{surf}	Surface classification (snow/ice, water, vegetated land, non-vegetated land) index number	none
i_{bright}	Scene brightness index number	none
i_{band}	MISR spectral band index number	none
i_{temp}	Temperature index number	none
$i_{bandrlra}$	"Combined" index number for band and altitude	none
Nominal view zenith angle cosines and solid angle bin boundaries		
μ_k	Values used in establishing the AZM weights. Values: 0.334, 0.500, 0.700, 0.898, 0.983, 0.898, 0.700, 0.500, 0.334 for μ_1 - μ_9	none

Table 5: Contents of the AZM Dataset (continued)

Parameter	Description	Units
$\mu_{k,lower}$ $\mu_{k,upper}$	Values used in establishing the solid angle bin boundaries on the "igloo", in the direction of view zenith angle cosine Values: 0.000, 0.417, 0.600, 0.799, 0.941, 0.799, 0.600, 0.417, 0.000 for $\mu_{1,lower}$ - $\mu_{9,lower}$; and 0.417, 0.600, 0.799, 0.941, 1.000, 0.941, 0.799, 0.600, 0.417 for $\mu_{1,upper}$ - $\mu_{9,upper}$	none
ϕ_{mean}	Values used in establishing the solid angle boundaries on the "igloo", in the direction of relative azimuth angle. Values (corresponding to the solar zenith angle bins): 65°, 65°, 65°, 65°, 50°, 50°, 35°, 35°, 30°, 30°, 25°, 25°, 20°, 20°, 20° if the D-camera viewing forward scattering has relative azimuth $\leq$ 90° 295°, 295°, 295°, 295°, 310°, 310°, 325°, 325°, 330°, 330°, 335°, 335°, 340°, 340°, 340° if the D-camera viewing forward scattering has relative azimuth $\geq$ 270°	degrees
Thresholds		
ξ_{sun}	Upper limits of solar zenith angle bins. Values: 20°, 25°, 30°, 35°, 40°, 45°, 50°, 55°, 60°, 65°, 70°, 75°, 80°, 85°, 90°	degrees
$\xi_{view\_zenith\_angle}$	Upper limits of view zenith angle index bins. Values: 7°, 20° for An; 29°, 32° for Af/Aa; 47°, 50° for Bf/Ba; 61°, 63° for Cf/Ca; 71.5°, 73° for Df/Da	degrees
ξ_{azim}	Upper limits of view-sun relative azimuth angle bins, dependent upon the solar zenith angle.	degrees
ξ_{alt}	Upper limits of the RLRA bins, with the number and values depending on spectral band: Blue: 2.2 km, 5.0 km, 9.7 km, 20.0 km Green: 5.2 km, 20.0 km Red/near-IR: Not applicable	km
ξ_{bright}	Upper limits of red band brightness (BRF) bins. Values correspond to homogeneous clouds with optical thicknesses of 3.75, 6.25, 8.75, 12.50, 17.50, 22.50, 27.50, 33.75, 41.25, 50.00, 60.00, 72.50, ∞, with 13 values for each combination of i_{sun}, $i_{view\_zenith\_angle}$, i_{azim}, i_{phase}, i_{surf}, and camera identifier k.	none

| Parameter	Description	Units
ξ_{text}	Thresholds on subregional cloud texture. Separate threshold for each combination of i_{sun}, $i_{view\_zenith\_angle}$, i_{azim}, i_{bright}, as well as each possible value of the homogeneity reference camera (An, Af/Aa, Bf/Ba).	none
ξ_{temp}	Upper temperature limits of bins for the probability of the presence of liquid cloud phase. Values: 0, -3, -7, -11, -15, -19, -23, -27, -31, -35, -39, and -43°C	°C
Cloud phase		
P_{liquid}	Probability of cloud phase = Liquid for clouds of Unknown phase	%
Deterministic modeling coefficients		
w_{kl}	Angular integration weights for all values of k, l for each model. Dependent upon i_{sun}, $i_{view\_zenith\_angle}$, i_{azim}, i_{band}, i_{alt}, i_{phase}, i_{surf}, i_{bright}, i_{igloo}, and camera identifiers k and l.	none
ε_k	Angular integration bias coefficients for all values of k for each model. Dependent upon i_{sun}, i_{azim}, i_{band}, i_{alt}, i_{phase}, i_{surf}, i_{bright}, i_{igloo}, and camera identifier k	none
Δ_d	Deterministic model agreement thresholds. Dependent upon i_{sun}, i_{azim}, i_{igloo}, i_{bright}, and camera identifiers k and l	none
Stochastic modeling coefficients		
w_{kl}	Angular integration weights for all values of k, l for each model. Dependent upon i_{sun}, $i_{view\_zenith\_angle}$, i_{azim}, i_{band}, i_{alt}, i_{phase}, i_{surf}, i_{igloo}, camera identifiers k and l.	none
ε_k	Angular integration bias coefficients for all values of k for each model. Dependent upon i_{sun}, i_{azim}, i_{band}, i_{alt}, i_{phase}, i_{surf}, i_{igloo}, and camera identifier k	none
σ_{kl}	Albedo contribution expected errors for all values of k, l for each model. Dependent upon i_{sun}, $i_{view\_zenith\_angle}$, i_{azim}, i_{igloo}, i_{band}, i_{surf}, i_{phase}, i_{alt}, and camera identifiers k and l.	none
Δ_s	Stochastic model agreement thresholds. Dependent upon i_{sun}, i_{azim}, i_{igloo}, i_{bright}, and camera identifiers k and l.	none
Solid angle weighting coefficients		

Parameter	Description	Units
c_k	Correction factors for neighboring angles that use Deterministic or Stochastic weighting, excluding c_5	none
w_{kl}	Local albedo angular integration weights for use with top-leaving BRF's, excluding w_{11}, w_{55}, and w_{99}	none
q_{kk}	Angular integration weights for determining effective BRF's in expansive albedo calculation, and for use with side-leaving BRF's in restrictive albedo calculation	none

4.2 PROCESSING OUTLINE

An overview of the processing flow concept for generation of the AZM Dataset at the SCF is shown in Figure 10.
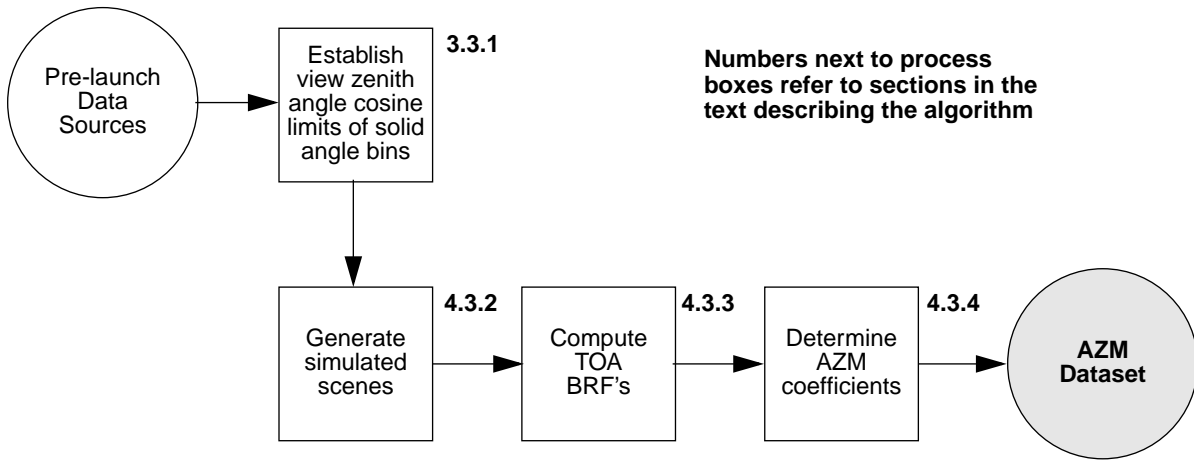
Figure 10. Conceptual processing flow for generation of the AZM Dataset

4.3 ALGORITHM INPUT

The main input to the radiative transfer modeling of cloud scenes is the three-dimensional distribution of cloud water, which in turn is often generated using a stochastic model which produces cloud fields that follow power-law scaling. A break in the power-law scaling, as noted by Barker and Davies *[1]*, is introduced for some of the scenes. Some cloud scenes are based directly on satellite observations, and both Landsat and AVHRR (LAC) data are used for this.

Within the cloud, drop size distributions follow the modified gamma distributions of Welch et al. *[32]* for liquid drops, and Takano and Liou *[26]* or Sassen and Liou *[24]* for randomly oriented hexagonal ice crystals. The non-cloud structure of the atmosphere adopts the model atmo-

spheres of LOWTRAN 7 *[17]*, and the Rayleigh extinction coefficients of Iqbal *[14]*.

4.4 THEORETICAL DESCRIPTION

4.4.1 Establish view zenith angle cosine limits on solid angle bins

The values of zenith angle cosine which define the limits of the solid angle bins (see §3.3.1) are determined as follows.

(1) The $k = 5$ bin is centered on $\mu = 1$. However, since the nadir camera has a field-of-view (FOV) of $\pm15°$, its zenith angle cosine varies from 1.000 at the center of the FOV to 0.966 at the edges. Thus, the nominal value for μ_5 is established as the mean of these values, or 0.983. The lower limit on the $k = 5$ bin is then given by $\frac{1}{2}(\mu_5 + \mu_4) = \frac{1}{2}(\mu_5 + \mu_6)$, where we note that the nominal values of μ_4 and μ_6 are identical. These values also establish the upper limits on bins 4 and 6.

(2) The lower limit on bin k, which is the same as the upper limit on bin k - 1, for $2 \leq k \leq 4$, is given by $\frac{1}{2}(\mu_{k-1} + \mu_k)$.

(3) The lower limit on bin k, which is the same as the upper limit on bin k + 1, for $6 \leq k \leq$ 8, is given by $\frac{1}{2}(\mu_{k+1} + \mu_k)$.

(4) The lower limit on bin 1 and bin 9 is $\mu = 0$.

4.4.2 Generate simulated scenes

For the simulated cloudy scenes, inherent nonlinearities and the high variability of cloud scenes require the use of numerical methods. Simulated plane-parallel and stochastic broken cloud fields are considered, as are internally homogeneous and inhomogeneous cloud elements within these cloud fields, as well as scenes based on Landsat and AVHRR LAC images. Details of the stochastic cloud generation scheme are given in Várnai *[29]*, summarized as follows:

(1) A 2-D Gaussian white noise of Fourier coefficients is generated;

(2) Power-law scaling of the coefficients as a function of wavenumber is applied;

(3) A 2-D inverse Fourier transform of the scaled coefficients is carried out;

(4) The resulting values are first multiplied by a certain number C, then exponentiated. If C is small, the resulting field will have a Gaussian thickness distribution, while the larger values of C yield more skewed distributions (multifractal cloud fields); and

(5) A threshold cut and a multiplication set the cloud fraction and the average thickness to their desired values. In order to enhance the variety of simulated cloud fields, the fourth step is sometimes replaced by an alternate step. This includes taking a power as well, with the power-base being an arbitrary number (> 1). The internal inhomogeneities (3-D variations of the volume extinction coefficients) are generated by a similar algorithm extended to three dimensions.

4.4.3 Compute TOA BRF's

TOA BRF's for cloudy scenes are based on 3-D Monte Carlo (MC) radiative transfer calculations, full details of which are given in Várnai [29]. Cloud particles in the Monte Carlo radiative transfer calculations may be either water droplets, hexagonal ice crystals, or a mixture of the two. For the water droplets, Mie calculations are used to obtain the single scattering properties for different drop size distributions. Modal radii range from 5 μm (St base) to 20 μm (C.6 precipitating cloud). The effects of overlying atmosphere and underlying surface are also included using standard models.

A comparison of Figures 11 and 12 shows that the azimuthal variation of BRF is influenced substantially by cloud properties. The values in the figures are in BRF units. Radial distance is proportional to the cosine of the view angle, and azimuthal angle has forward scattering to the left. The main factors determining the azimuthal dependence of cloud reflection are solar elevation, cloud thickness and structure, and the single-scattering properties of cloud particles. Figures 11 and 12 also reveal features common to most clouds: reflection peaks in forward and/or backscatter directions. These peaks are due to respective peaks in the scattering phase function of cloud particles and, if present, to cloud inhomogeneities [7].

Use of Solid Angle Weighting alone can lead to biases in albedo estimation, which are due mainly to these peaks. For example, if MISR measures near the solar plane, the scheme assumes that the high reflectance values detected by oblique cameras occur over all azimuths, and thus overestimates the true albedo. If, however, MISR measures far from the solar plane, the scheme completely ignores the existence of peaks, and thus underestimates the real albedo. An example of such biases is shown in Figure 13. The bias errors are negligible for small solar zenith angle, irrespective of azimuthal plane, and minimal at relative azimuthal angles $\approx 45°$ for most solar zenith angles.
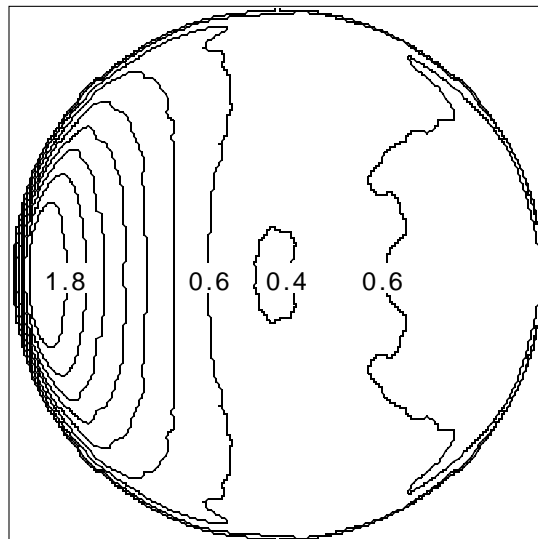
Figure 11. Angular dependence of the reflected radiation for 60° solar zenith angle: plane-parallel cloud with optical depth $\tau = 7.5$ and albedo = 0.55
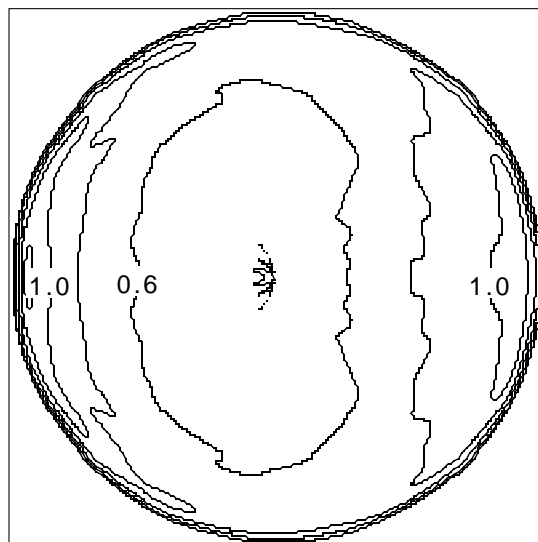
Figure 12. Angular dependence of the reflected radiation for 60° solar zenith angle: broken cloud field with the same scene-average albedo
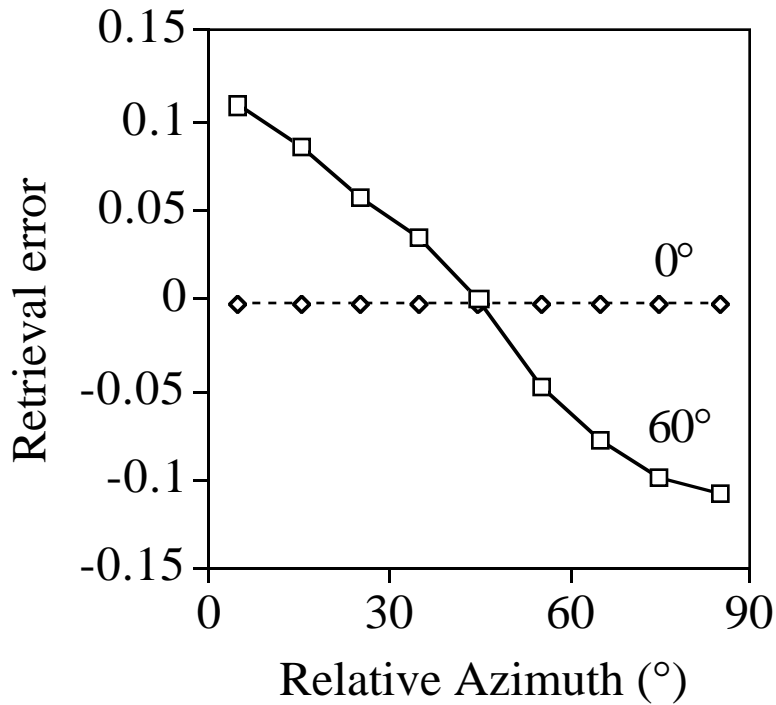
Figure 13. Azimuth-dependent bias of the Solid Angle Weighting scheme for a plane-parallel cloud with τ = 7.5. The solar zenith angles are 0° and 60° for the two curves, respectively

The biases shown in Figure 13 can only be avoided by using more realistic angular models for cloud reflection. There are two main approaches for generating such models. The first approach is to use theoretical cloud models. This strategy has been followed by the International Satellite Cloud Climatology Project (ISCCP), which used plane-parallel cloud models in satellite retrievals *[23]*. The second approach is to combine large numbers of observations from various view angles to obtain "average" angular distributions. This statistical approach has been chosen in the Earth Radiation Budget Experiment (ERBE) *[27]*.

The sun-synchronous orbit of EOS-AM satellites prohibits using the statistical approach. The problem is the correlation between solar elevation and the relative azimuth of MISR-measurements. For example, all MISR measurements for 60° solar zenith angle will be about 20° - 30° off the solar plane, while reflection to larger azimuths will never be measured. Thus, even if one used the principle of reciprocity *[28]*, there would be no data with which to construct a reflection model for oblique views at large azimuth angles.

4.4.4   Determine AZM coefficients

4.4.4.1   Deterministic and stochastic weights

The theoretical development leading to the choice of the deterministic and stochastic weights for cloudy scenes is described in detail in Várnai *[29]*, a summary of which follows here. There are two main steps: calculating the radiative properties of a large variety of cloud scenes, and using the results to generate the required coefficients. These steps are described in the following two subsections.

4.4.4.1.1   Cloud database

The main purpose of generating the cloud database is to obtain the radiative properties of a wide variety of cloud fields. The scenes in the database are specified by satellite retrievals and by a stochastic cloud model described in §4.4.2. The scenes, at 68-meter resolution, cover 35.2 x 35.2 km areas (the resolution of coarse MISR albedos), and include a large variety of

- Cloud thicknesses (optical depths ranging from 1.5 to 50),

- Cloud structures (including homogeneous, plane-parallel clouds and broken cloud fields with both cloud top height and volume extinction coefficient variations), and

- Cloud microphysical properties (based on various dropsize and ice crystal distributions).

The homogeneous cloud portion of the database contains a separate scene for each cloud model used in deterministic retrievals. The thickness and altitude of these scenes is chosen to ensure that retrieval errors due to variations in these properties remain below 0.01. The scenes required for this level of accuracy are selected by using Monte Carlo simulations to estimate the uncertainty of retrievals that use various sets of homogeneous clouds as their database.

About half of the inhomogeneous scenes in the database are retrieved from satellite images. These scenes are representative of various types of inhomogeneous clouds, such as marine stratocumulus and cumulus. The rest of the scenes are generated by the stochastic model described in §4.4.2. Since there are no data available on the global distribution of structural cloud parameters, the model-generated scenes complement the satellite images to obtain a relatively uniform distribution of structural cloud properties.

Cloud radiative properties are calculated using the Monte Carlo model described above. Presently, the database includes results for 84 cloud fields at 446 nm and 866 nm wavelengths (blue and near-infrared MISR channels). At this time, results have been generated for 0°, 30°, 60° and 80° solar zenith angles, but simulations for other solar zenith angles are in process. Atmospheric

effects as described above are also included. A technique similar to the adding-doubling method ensures that the available Monte Carlo results can be used to calculate cloud reflection above any surface in a matter of seconds. Cloud reflection is calculated at an angular resolution of 10° along the azimuth and 0.04 along the cosine of the viewing zenith angle. In order to obtain fairly high accuracies (with errors typically less than 0.01 in reflectance and 0.0003 in albedo values), each Monte Carlo experiment has simulated at least four million photons. Thus the main uncertainties of the cloud dataset are not in calculating radiative transfer, but in specifying the cloud fields in a realistic way. In particular, the main limitations, in approximate order of importance, are that

- The dataset is based largely on artificial cloud structures, and it is unknown how representative each cloud field is of real ones,

- The microphysical properties of ice crystals are poorly known and hence may not be well represented,

- The large variety of underlying surfaces is not fully represented,

- Water cloud microphysics is simplified by using only a few dropsize distributions,

- The dataset is based on LOWTRAN model atmospheres which are not representative of all atmospheric conditions,

- Light polarization and atmospheric refraction are neglected.

Future MISR measurements may be used to reduce the uncertainties due to the first and most important problem. Currently, there is no reliable way to tell the degree to which particular artificially generated cloud fields are representative of real cloud fields, and thus each one is given equal weight in various calculations based on the dataset. However, these equal weights may be modified using future MISR measurements. For example, a large number of MISR measurements could each be assigned to the most similar cloud model in the dataset. Then each cloud field in the dataset would be given a weight proportional to the number of measurements assigned to it. Once these weights were calculated, the new dataset could be used to refine the albedo retrieval method. However, since no MISR measurements are presently available, the details of such possible improvements have not yet been developed.

4.4.4.1.2   *Azimuthal Models*

Once the cloud dataset is set up, the next task is to generate azimuthal models (AZM's), i.e., to determine the integration coefficients. After various methods were tested, the following algorithms proved to be best.

The w_{kl} and ε_k values for the Deterministic methodology are calculated using the following

algorithm:

(1) An initial guess for the w_{kl} values, denoted w'_{kl}, is obtained using

$$w'_{kl} = \frac{\langle \delta A_k \rangle}{\langle \overline{B_l} \rangle} \tag{55}$$

where $\langle\ \rangle$ indicates averaging over N_{scenes}, the number of relevant scenes in the cloud dataset. The δA_k and $\overline{B_l}$ values are established from the Monte Carlo radiative transfer simulations described in §4.4.4.1.1.

(2) $\delta A'_{kl,i}$, a first-order estimate of $\delta A_{k,i}$ is obtained for each scene:

$$\delta A'_{kl,i} = w'_{kl}\overline{B_{l,i}} \qquad i = 1, 2, ..., N_{scenes} \tag{56}$$

(3) The calculation in step (2) does not take into account that cloud reflection becomes more isotropic as clouds become thicker, which could lead to biases in the retrieved albedo values (see below). This also introduces artificial jumps in the retrieved albedo values in case of clouds that are near the border of two cloud models of different brightness. These problems are corrected by using a linear regression over all relevant scenes:

$$\delta A_{k,i} = \eta_k(\delta A'_{kl,i}) + \varepsilon_k \tag{57}$$

which is used to determine values for η_k and ε_k. To avoid erroneous regression results, the η_k is limited to the range between 0.95 and 1.05. The values of ε_k in the AZM Dataset are obtained from Eq. (57), and the values of w_{kl} are obtained from:

$$w_{kl} = \eta_k w'_{kl} \tag{58}$$

The w_{kl}, ε_k, and σ_{kl} values for the Stochastic methodology are calculated using the following algorithm:

(1) An initial guess for the w_{kl} values, denoted w'_{kl}, is obtained using

$$w'_{kl} = \frac{\langle \delta A_k \rangle}{\langle \overline{B_l} \rangle} \tag{59}$$

where $\langle\ \rangle$ indicates averaging over N_{scenes}, the relevant scenes in the cloud dataset. The δA_k and $\overline{B_l}$ values are established from the Monte Carlo radiative transfer simulations described in §4.4.4.1.1.

(2) $\delta A'_{kl, i}$, a first-order estimate of $\delta A_{k, i}$ is obtained for each scene:

$$\delta A'_{kl, i} = w'_{kl} \overline{B_{l, i}} \qquad i = 1, 2, ..., N_{scenes} \tag{60}$$

These estimations have RMS errors σ_{kl}, which are weighted according to the distance between the camera numbers k and l and are stored in the AZM Dataset. They are given by:

$$\sigma_{kl} = \frac{1}{N_{scenes}} \sqrt{\sum_{i=1}^{N_{scenes}} (\delta A'_{kl, i} - \delta A_{k, i})^2} \tag{61}$$

where $\delta A_{k, i}$ is the "true" value for the ith scene in the cloud database. The values are then combined using

$$\delta A'_{k, i} = \frac{1}{9} \sum_{l=1}^{9} \delta A'_{kl, i} \tag{62}$$

(3) The calculation in step (2) does not take into account that cloud reflection becomes more isotropic as clouds become thicker. Thus, the estimated $\delta A'_{k, i}$ values are biased downward for thin clouds, and upward for thick clouds. This bias can be eliminated through the use of a simple linear regression over all relevant scenes in the cloud database:

$$\delta A_{k, i} = \eta_k (\delta A'_{k, i}) + \varepsilon_k \tag{63}$$

which is used to determine values for η_k and ε_k. The values of ε_k in the AZM Dataset are obtained from Eq. (63), and the values of w_{kl} are obtained from:

$$w_{kl} = \eta_k w'_{kl} \tag{64}$$

Figure 14 shows that the linear regression methodology described above effectively reduces the cloud thickness-dependent bias even if the stochastic method is used to retrieved the albedo of homogeneous clouds of various thicknesses.
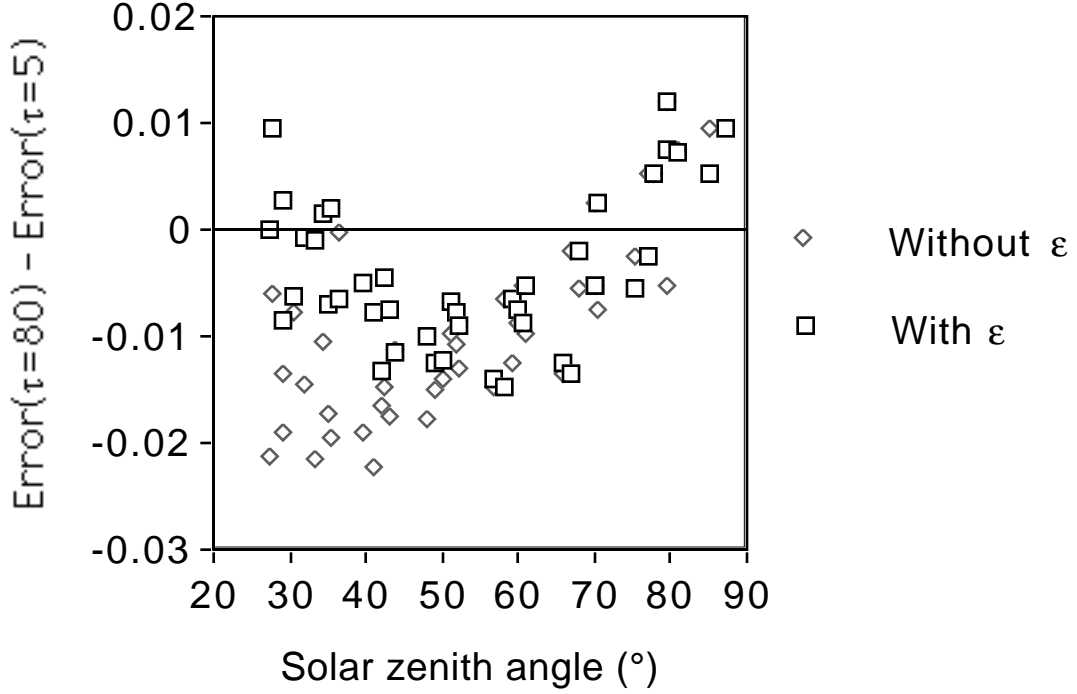
Figure 14. Difference between retrieval errors if the albedo of homogeneous clouds with $\tau =$ 80 and $\tau = 5$ is retrieved using stochastic modeling

4.4.4.2   Solid angle weights

4.4.4.2.1   Correction factors when neighboring angles use cloud models

Calculation of δA_k by Solid Angle Weighting uses the average BRF's at angle k and neighboring angles. However, if the index l of the neighboring angle corresponds to an angle at which either the Deterministic or Stochastic method has been successfully used, the calculation incorporates the albedo contribution for that angle divided by the unobscured fraction and a correction factor c_l (see §3.4.2.3). The c_l values are given by:

$$c_1 = \frac{1}{8}(\mu_2^2 + \mu_1^2 + 2\mu_1\mu_2) \tag{65}$$

$$c_l = \frac{1}{8}(\mu_{l+1}^2 - \mu_{l-1}^2 + 2\mu_l\mu_{l+1} - 2\mu_l\mu_{l-1}) \qquad 1 < l < 5$$

$$c_l = \frac{1}{8}(\mu_{l-1}^2 - \mu_{l+1}^2 + 2\mu_l\mu_{l-1} - 2\mu_l\mu_{l+1}) \qquad 5 < l < 9$$

$$c_9 = \frac{1}{8}(\mu_8^2 + \mu_9^2 + 2\mu_8\mu_9)$$

66

where a value of c_5 is not needed because the Deterministic or Stochastic methods are never used for this camera.

4.4.4.2.2 Weights for local albedo calculations

The coefficients used in the Solid Angle Weighting method for top-leaving BRF's in the calculation of local albedos (§3.4.2.3) are found algebraically as follows, using trapezoidal integration and assuming continuity in $\mu_k u_k \overline{b}_k$ between measured values. Note that values for w_{11}, w_{55}, and w_{99} are not included, as these must be determined during the retrievals.

For $k = 1$,

$$w_{12} = \frac{\mu_2}{8}(\mu_2 - \mu_1) \tag{66}$$

For $1 < k < 5$,

$$w_{k, k-1} = \frac{\mu_{k-1}}{8}(\mu_k - \mu_{k-1}) \tag{67}$$

$$w_{kk} = \frac{3\mu_k}{8}(\mu_{k+1} - \mu_{k-1}) \, , \tag{68}$$

$$w_{k, k+1} = \frac{\mu_{k+1}}{8}(\mu_{k+1} - \mu_k) \tag{69}$$

For $k = 5$,

$$w_{54} = \frac{\mu_4}{8}(\mu_5 - \mu_4) \tag{70}$$

$$w_{56} = \frac{\mu_6}{8}(\mu_5 - \mu_6) \tag{71}$$

For $5 < k < 9$,

$$w_{k, k-1} = \frac{\mu_{k-1}}{8}(\mu_{k-1} - \mu_k) \tag{72}$$

$$w_{kk} = \frac{3\mu_k}{8}(\mu_{k-1} - \mu_{k+1}) \tag{73}$$

$$w_{k,\,k+1} = \frac{\mu_{k+1}}{8}(\mu_k - \mu_{k+1}) \tag{74}$$

For $k = 9$,

$$w_{98} = \frac{\mu_8}{8}(\mu_8 - \mu_9) \tag{75}$$

4.4.4.2.3   Weights for restrictive and expansive albedo calculations

A different set of solid angle weights is determined by assuming that the product of view zenith angle cosine, obscuration factor, and BRF varies linearly between one value of k and the next. These are used for calculating the contribution of side-leaving BRF's to restrictive albedo (§3.5.1.2) and in establishing effective top-leaving BRF's in the calculation of expansive albedo (§3.6.1). The values are given by:

$$q_{11} = \frac{\mu_1\mu_2}{2} \tag{76}$$

$$q_{kk} = \frac{1}{2}(\mu_k\mu_{k+1} - \mu_k\mu_{k-1}) \qquad 1 < k < 5 \tag{77}$$

$$q_{55} = \frac{1}{2}(2 - \mu_4\mu_5 - \mu_5\mu_6) \tag{78}$$

$$q_{kk} = \frac{1}{2}(\mu_k\mu_{k-1} - \mu_k\mu_{k+1}) \qquad 5 < k < 9 \tag{79}$$

$$q_{99} = \frac{\mu_8\mu_9}{2} \tag{80}$$

These weights refer to the total contribution of the measured value from the kth camera to the albedo, not just the contribution from the solid angle bin centered on the measurement. Therefore, they are subtly different from the weights used for local albedo calculations.

4.5   VARIANCE OR UNCERTAINTY ESTIMATES

4.5.1   Cloudy scenes

Since no measurements similar to MISR are available, the uncertainties of the albedo-retrieval method can be estimated only from the present cloud dataset. However, since this dataset is largely made up of artificially generated cloud fields, uncertainty estimates should only be considered as guides, not as quantitatively reliable values. It is nonetheless worthwhile to make estimates

to test whether the retrieval algorithms behave reasonably, and to demonstrate the potential benefits of using multiple views for albedo retrievals. These two tasks are addressed by using the Azimuthal Models derived from the cloud dataset to retrieve albedos for various scenes in the dataset.

The error estimates are presented for MISR band 4. For the sake of simplicity, all results presented are for non-reflecting surfaces (which might be regarded as a first-order approximation for oceans). Over oceans, the most important difference between the four channels is in the magnitude of Rayleigh scattering. The main effect of this scattering is to smooth out the differences among the angular distributions of radiation reflected by various cloud types, thus making albedo retrievals slightly easier. Therefore, MISR cloud albedo retrievals are expected to be most accurate for band 1 and least accurate for band 4. The difference between retrieval accuracies at these two wavelengths is demonstrated at the end of §4.5.1.2.

4.5.1.1   Testing the behavior of retrieval algorithms

The logic of plane-parallel and generic cloud albedo retrieval methods ensures that they are free from an overall bias. That is, given a perfect cloud database, they can correctly determine the global average albedo of their respective scenes. The lack of overall bias does not, however, necessarily imply that they could not have systematic biases for various cloud types. For example, such a bias could be a systematic over- and under-estimation of albedo values according to various cloud dropsize distributions. Such a bias would mean, for example, that the albedos obtained for fogs (made up of very small droplets) would all be biased upward or downward. The average errors for various dropsize distributions, shown in Figure 15, however, indicate that this is not the case: neither plane-parallel nor generic cloud retrievals lead to significant dropsize-dependent biases. In this figure, the relative azimuth is 60° for solar zenith angle = 30°, and 30° for solar zenith angle = 60° and 80°. These azimuth values are representative of the orbit of the EOS-AM satellite and are used in subsequent figures as well. Since only two ice phase functions are presently available, and it is not clear how representative they are of real ice clouds, the effects of cloud phase cannot yet be estimated in a reliable way. Therefore, the problem of ice clouds should be addressed in future studies.
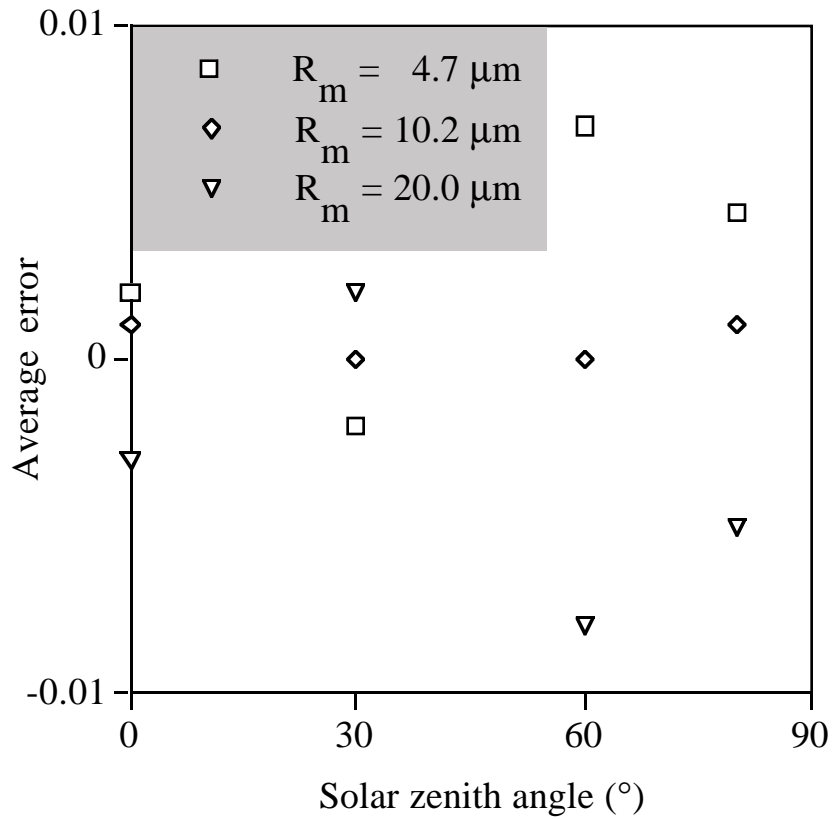
Figure 15. Average albedo retrieval errors for plane-parallel clouds having modified gamma dropsize distributions with various modal radii

Another bias in generic cloud retrievals could be over- or underestimation of cloud albedos, depending on whether a scene was nearly plane-parallel or very inhomogeneous. The possibility of such a bias is examined by using coefficients from generic cloud models to estimate the albedos of plane-parallel clouds. It is expected that if the albedo values for plane-parallel clouds are biased either way, albedos for very broken cloud scenes must be biased in the opposite direction in order to allow the overall average to remain correct. The results shown in Figure 16 suggest this bias to be fairly small, and certainly much smaller than it would be for single-view instruments.
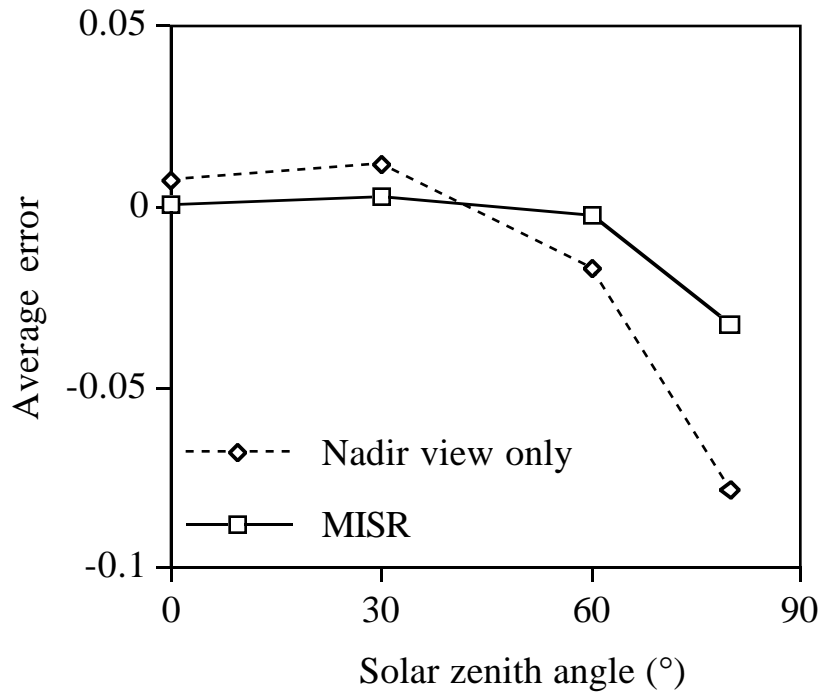
**Figure 16. Average error if the albedo of plane-parallel clouds is retrieved using generic cloud models**

4.5.1.2   Benefits of using multiple views

Multiple views can improve retrieval accuracies in two ways. First, knowledge of the angular variation of reflected radiation helps decide whether or not plane-parallel or generic cloud models can be used, and thereby prevents the use of inappropriate models in certain cases. The importance of this is shown in Figure 17.
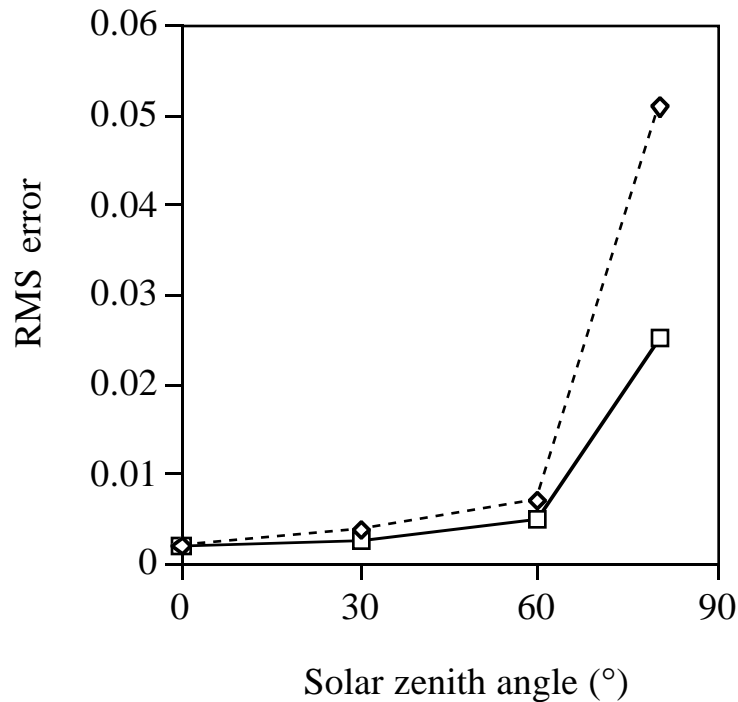
Figure 17. RMS error of estimates for inhomogeneous cloud albedos obtained using various cloud models and all nine cameras. The dashed line indicates results if plane-parallel models are used for the retrievals; the solid line, if the generic cloud model is used

Multiple views also decrease errors once the appropriate retrieval method is selected. To examine this effect, the RMS errors of albedo estimations based on all nine views are compared to errors that would occur if the nadir view alone were available. For plane-parallel clouds, the accuracy of angular integration cannot improve significantly, since for such scenes even nadir-only measurements can give accurate results (for water clouds with RMS errors less than 0.005). Hence, for homogeneous scenes, multiple views can decrease albedo retrieval errors mainly by reducing non-systematic calibration errors and random noise in the measurements. For inhomogeneous clouds, however, multiple views can improve the accuracy of angular integration significantly, as shown in Figure 18. This result is very important, since it indicates that MISR will be able to achieve one of its main goals, to improve the accuracy of albedo retrievals for inhomogeneous clouds. Figure 18 also shows that the improvement is greatest for oblique sun cases -- exactly where single-view retrievals are least accurate.
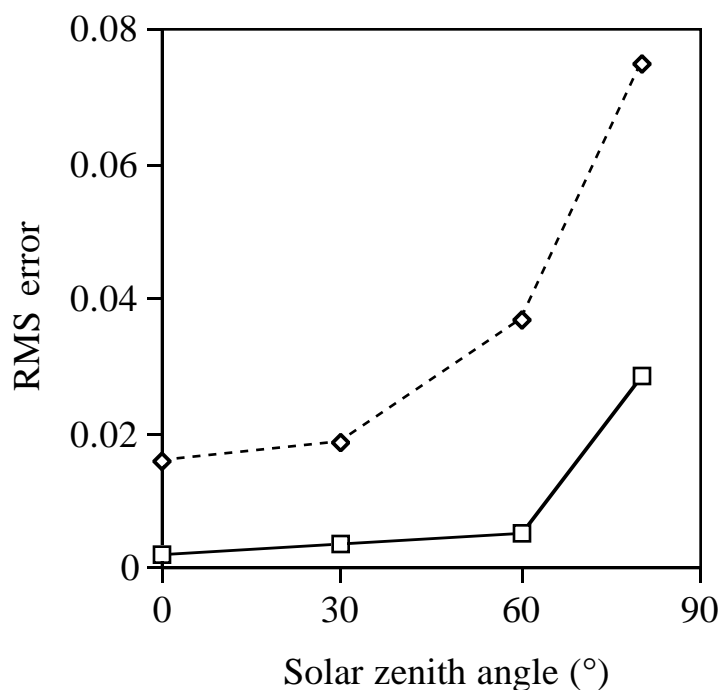
Figure 18. RMS error of stochastic albedo retrievals using a single nadir view (dashed line) and nine views (solid line). Since the results are obtained for 35.2 x 35.2 km areas, they represent the accuracy of coarse albedos

Since Figure 18 presents error estimates obtained at 35.2 km resolution, its values refer to coarse albedos. With regard to local albedos, their accuracy can be affected by some 2.2 km pixels containing only portions of inhomogeneous clouds. In order to demonstrate this, the reflection of a 35.2 x 35.2 km broken cloud field of optical depth 15 was simulated at 2.2 km resolution. For 60° solar zenith angle, the results indicate that while the generic cloud model can determine the overall scene albedo with an error of only 0.017, the RMS error for the local subregions is 0.047. This indicates that MISR's local albedo values have larger uncertainties than coarse albedos. Since using a single nadir view for the same scene would give a local albedo uncertainty of 0.134, though, MISR's multiple views can still be expected to improve the accuracy of local albedos.

A way to look at how each camera affects final retrieval accuracy is to examine how errors change as more and more oblique cameras are obscured. Figure 19 indicates that even if only the *A* and *B* cameras can be used, the accuracy is still significantly higher than that of nadir-only instruments.

73
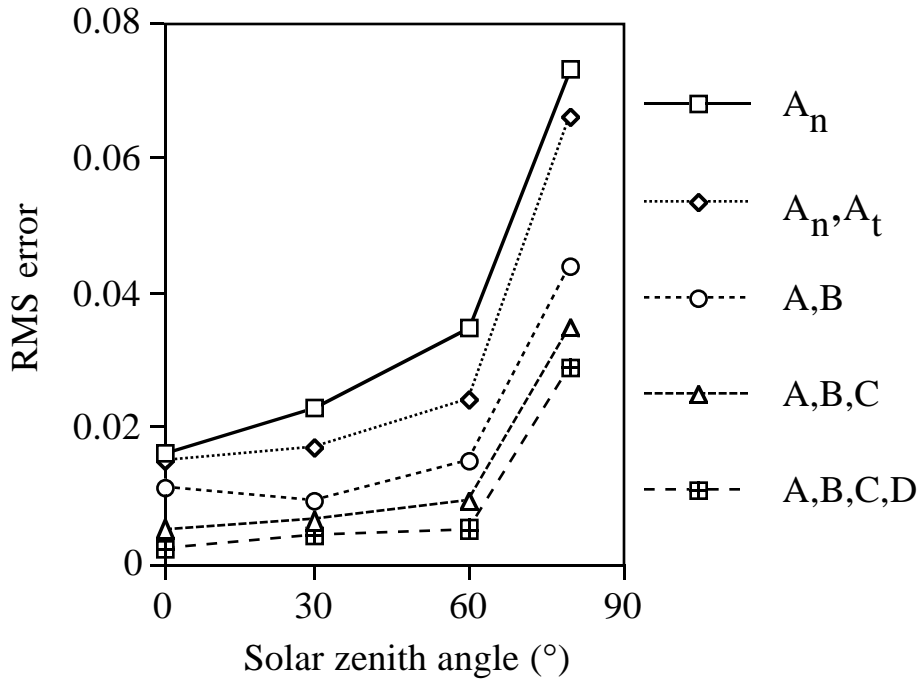
Figure 19. RMS errors if oblique cameras are obscured. Each line corresponds to a set of available cameras

Uncertainties associated with the Solid Angle Weighting scheme are much more difficult to evaluate than errors in plane-parallel and generic cloud retrievals. The reason for this is that the cloud database cannot be used to test the scheme, since the scheme is supposed to be applied specifically for cases that are inconsistent with the database contents. Until actual measurements can be studied, it is reasonable to expect that multiple views will improve the retrieval accuracy even for the Solid Angle Weighting scheme.

So far, all estimates for the retrieval uncertainty have been presented for the 866 nm MISR band. As mentioned above, the most important difference over ocean between the four channels is in the magnitude of Rayleigh scattering. The main effect of this scattering is to smooth out the differences among the angular distributions of radiation reflected by various cloud types, thus making albedo retrievals easier. This effect is examined by comparing the accuracy of albedo retrievals at a wavelength with strong Rayleigh scattering (446 nm) to the accuracy at a wavelength with negligible Rayleigh effect (866 nm). The results presented in Figure 20 suggest that MISR albedos can be expected to be most accurate for the blue channel. Over land, however, we note that the retrieval accuracy at various wavelengths depends on how precisely the surface characteristics are known.
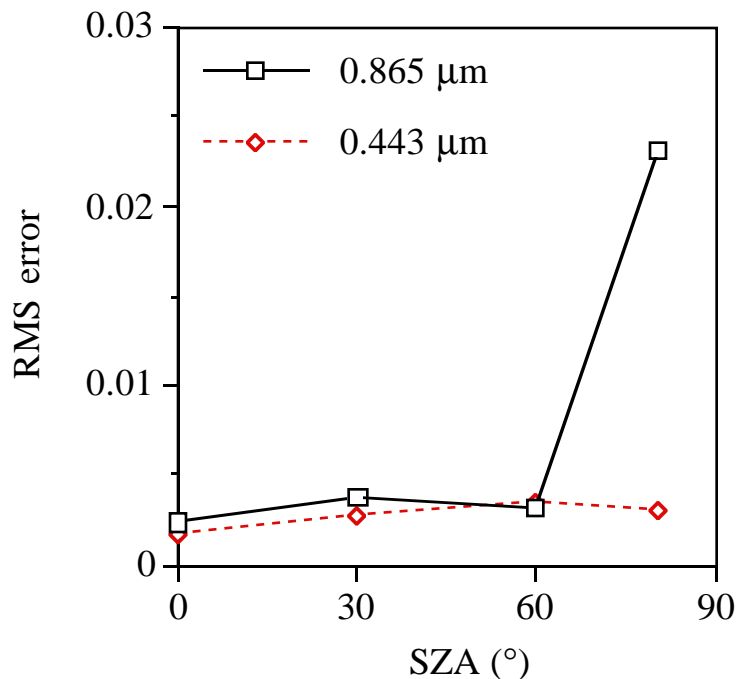
**Figure 20. RMS error of stochastic albedo retrievals in MISR bands 1 and 4**

4.5.2 Clear scenes

To test the accuracy of the Deterministic approach for clear scenes, simulated scenes using a variety of surface bidirectional reflectance characteristics overlain by atmospheric models were generated. Surface bidirectional reflectance distribution functions (BRDF) are based on the Pinty and Verstraete *[21]* and Iaquinta and Pinty *[13]* models, as well as field data of Kimes et al. *[15]*, *[16]*. Water surfaces are modeled using a modified Cox-Munk model *[4]*. Other surface models, e.g., for soil, sand, snow, and ice are based on Kimes data, the Hapke model *[12]*, and the Minnaert model *[19]*. The Pinty-Verstraete model or the Iaquinta-Pinty model for vegetation and the modified Cox-Munk model are used to compute both the spectral reflectance for a given wavelength and the BRDF. However, the Hapke model, the Minnaert model and the Lambertian model give a BRDF but no spectral reflectance for a selected wavelength. Thus we apply a scaling procedure, using the 6S code *[30]* to define a spectral albedo model for vegetation, soil or sand, clear and lake water. Reflectance values for snow and clean and dirty ice were taken from Gratton et al. *[11]*. For the clear sky atmospheric models, aerosol scattering functions for arctic, desert, clean maritime, average continental, and urban conditions were taken from d'Almeida *[5]*. TOA radiances for clear scenes are then calculated using a radiative transfer code based on the Grant-Hunt matrix operator method *[10]*, *[18]*.

The standard deviation σ of the albedo values was computed over all cases, dividing them

into general surface classes of: △ Vegetation (23 models), ◊ Soil and sand (3 models), + Snow and ice (9 models) and * Water (11 models), where the plot symbols shown are used in Figure 21. Each surface model was used with 5 different atmospheres and 3 sun angles. Thus a total of 690 TOA BRF's were inverted for 4 different MISR orbit azimuthal angles at (0°, 30°, 60° and 90°). Including all 4 spectral bands, this data set grows to 11,040 simulated MISR cases.

In Figure 21 we show the standard deviation of the albedo values computed with the model of §3.4.2.2.1 as compared with the calculated "true" albedos for all simulated MISR cases. The Rayleigh pre-correction is included. Most albedo errors lie between 1% and 2% (where a 1% error signifies an absolute albedo error of 0.01), though there are a few outliers for water in the red and near-infrared bands.
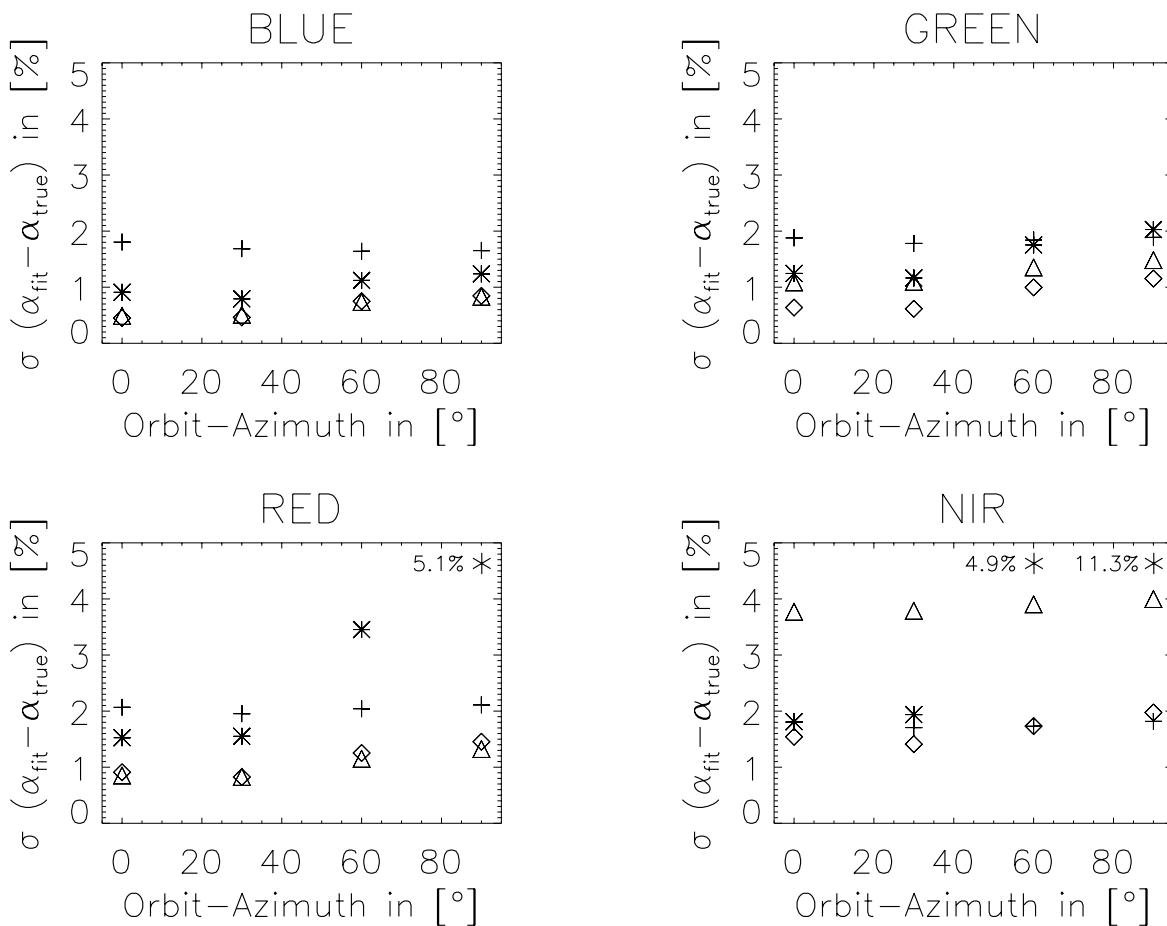
Figure 21. RMS albedo errors for clear scenes

Combining the results from all azimuth angles together, we obtain the summary statistics shown in Table 6.

Table 6: Summary of clear-scene results

Standard Deviation σ				
Channel	Surface			
	Water	Vegetation	Soil	Snow/ice
Blue	0.0103	0.0066	0.0066	0.0170
Green	0.0159	0.0127	0.0090	0.0186
Red	0.0328	0.0107	0.0118	0.0207
Near-IR	0.0638	0.0387	0.0170	0.0180

5. ASSUMPTIONS AND LIMITATIONS

5.1 ASSUMPTIONS

The following assumptions are made with respect to the top-of-atmosphere/cloud retrievals described in this document:

(1) MODIS Level 2 cloud phase will be available for incorporation into the systematic processing of MISR data.

5.2 LIMITATIONS

The following limitations apply to the at-launch top-of-atmosphere/cloud retrievals described in this document:

(1) The expansive albedos at the edges of the swath have larger uncertainties than in the interior of the swath due to fewer contributing measurements.

6. REFERENCES

[1] Barker, H. W. and J. A. Davies (1992). Cumulus cloud radiative properties and the characteristic of satellite radiance wavenumber spectra. *Rem. Sens. Env.* **42**, 51–64.

[2] Bevington, P.R. (1969). *Data reduction and error analysis for the physical sciences.* McGraw-Hill, Inc., 336 pp.

[3] Borel C.C., C. Tornow C. and S. A. W. Gerstl (1994). MISR quarterly report, July, (available on request from LANL).

[4] Cox, C. and W. Munk (1954). Measurements of the roughness of the sea surface from photographs of the Sun's glitter. *Jour. Opt. Soc. of Am.* **44**, 838.

[5] d'Almeida, G. A., P. Koepke, and E. P. Shettle (1991). Atmospheric Aerosols: Global climatology and radiative characteristics. Deepak Publishing.

[6] Di Girolamo, L. and R. Davies (1994). A Band-Differenced Angular Signature technique for cirrus cloud detection. *IEEE Trans. Geosci. Rem. Sens.* **32**, 890-896.

[7] Davies, R. (1984). Reflected solar radiances from broken cloud scenes and the interpretation of scanner measurements. *J. Geophys. Res.* **89**, 1259.

[8] Engelsen, O., B. D. Pinty, and M. M. Verstraete (1996). Parametric Bidirectional Reflectance Factor (BRF) models: I. Evaluation. Internal report, Institute for Remote Sensing Applications, Joint Research Centre, Ispra, Italy.

[9] Goel, N.S. (1988). Models of vegetation canopy reflectance and their use in estimation of biophysical parameters from reflectance data. *Remote Sensing Reviews* **4**, 1-222.

[10] Grant, I.P. and G.E. Hunt (1968). Solution of radiative transfer problems using the invariant S_n method. *Mon. Not. Royal. Astron. Soc.* **141**, 27-41.

[11] Gratton, D. J., P. J. Howarth and D. J. Marceau (1993). Using Landsat-5 Thematic Mapper and digital elevation data to determine the net radiation field of a mountain glacier. *Remote Sens. Environ.* **43**, 315-331.

[12] Hapke, B.W. (1981). Bidirectional reflectance spectroscopy. 1. Theory. *J. Geophys. Res.* **86,** 3039.

[13] Iaquinta, J. and B. Pinty (1994). Adoption of a bidirectional reflectance model including the hot-spot to an optical thin canopy. Proc. VI. Intern. Colloquium: Physical Measurements and

Signatures in Remote Sensing, Val d'Isere, France, January 17-21.

[14] Iqbal, M. (1983). *An Introduction to Solar Radiation*. Academic Press, 390 pp.

[15] Kimes, D.S., W.W. Newcomb, R.F. Nelson, and J.B. Schutt (1985a). Directional reflectance distributions of a hardwood and pine forest canopy. *IEEE Trans. Geosci. Remote Sens.* **GE-24**, 281-293.

[16] Kimes, D.S., W.W. Newcomb, C.J. Tucker, et al. (1985b). Directional reflectance factor distributions for cover types of Northern Africa in NOAA 7/8 AVHRR Bands 1 and 2. *Remote Sens. Environ.* **18**, 1-19.

[17] Kneizys, F.X., E.P. Shettle, W.O. Gallery, J.H. Chetwynd, Jr., L.W. Abreau, J.E.A. Selby, R.W. Fenn and R.A. McClatchey (1980). *Atmospheric Transmittance / Radiance: Computer Code LOWTRAN 5.* AFGL-TR-80-0067, *Environmental Research Papers* **697**, Air Force Geophysics Laboratory, 233 pp.

[18] Martonchik, J. V. (1975). Sulphuric acid cloud interpretation of the infrared spectrum of Venus. Ph. D. Thesis, University of Texas, Austin.

[19] Minnaert, M. (1941). The reciprocity principle in lunar photometry. *Astrophys. J.* **93**, 403.

[20] Oreopoulos, L. and R. Davies (1996). Plane parallel albedo biases from satellite observations. Part I: Dependence on resolution and other factors. *J. Climate* (submitted).

[21] Pinty, B. and Verstraete, M. M. (1991). Extracting information on surface properties from bidirectional reflectance measurements. *J Geophys. Res.* **96**, 2865.

[22] Rahman, H., B. Pinty, and M.M. Verstraete (1993). Coupled surface-atmosphere reflectance (CSAR) model 2. Semiempirical surface model usable with NOAA Advanced Very High Resolution Radiometer data. *J. Geophys. Res.* **98**, 20,791-20,801.

[23] Rossow, W.B., F. Mosher, E. Kinsella, A. Arking, M. Desbois, E. Harrison, P. Minnis, E. Ruprecht, G. Seze, C. Simmer, and E. Smit (1985). ISCCP cloud algorithm intercomparison. *J. Clim. Appl. Met.* **24**, 877.

[24] Sassen, K. and K.-N. Liou (1979). Scattering of polarized laser light by water droplet, mixed-phase and ice crystal clouds. Part I: Angular scattering patterns. *J. Atmos. Sci.* **36**, 838-851.

[25] Schiffer, R. A. and W. B. Rossow (1983). The International Satellite Cloud Climatology Project (ISCCP): The First Project of the World Climate Research Program (WCRP). *Bull. Amer.*

Met. Soc. **64**, 779.

[26] Takano, Y., and K-N Liou (1989). Solar radiative transfer in cirrus clouds. Part I: Single-scattering properties of hexagonal ice crystals. *J. Atmos. Sci.* **46**, 3-19.

[27] Taylor, V. R. and L. L. Stowe (1982). Reflectance characteristics of uniform Earth and cloud surfaces derived from Nimbus-7 ERB. *J. Geophys. Res.* **89***, 4987.

[28] van de Hulst, H. C. (1981). Light scattering by small particles. Dover Publications, Inc., NY.

[29] Várnai, T. (1996). Reflection of solar radiation by inhomogeneous clouds. Ph.D Thesis, McGill University, Montreal, 146 pp.

[30] Vermote, E., D. Tanre, J. L. Deuze, M. Herman and J. J. Morcrette (1994). Second simulation of the satellite signal in the solar spectrum (6S). User Manual.

[31] Vermote E. and D. Tanre (1992). Analytical expression for radiative properties of planar Rayleigh scattering media, including polarization contribution. *J. Quant. Spectrosc. Radiat. Transfer* **47**, 305-314.

[32] Welch, R.M., S.K. Cox and J.M. Davis (1980). *Solar Radiation and Clouds. Meteorological Monographs* **17**, #39, American Meteorological Society, 96 pp.